

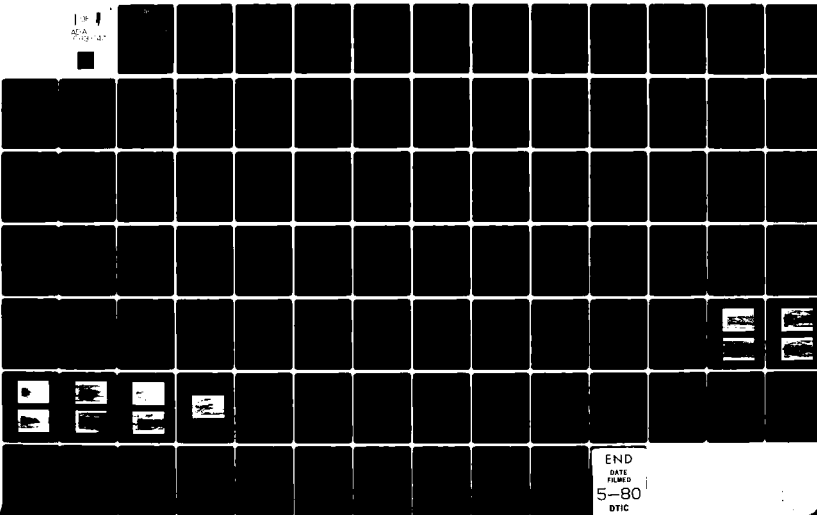
0-A083 047 MISSISSIPPI UNIV UNIVERSITY DEPT OF MECHANICAL ENGIN--ETC F/6 20/5
AN INVESTIGATION OF TURBULENT MIXING IN THE CHEMICAL LASER USIN--ETC(U)
DEC 79 C R WIMBERLY DAAG29-76-G-0044

UNCLASSIFIED

ARO-13224.1-E

NL

139
AFIA
7-10-81



END
DATE
FILED
5-80
DTIC

ADA 083047

LEVEL

ARO 13224.1-E



AN INVESTIGATION OF TURBULENT MIXING IN THE CHEMICAL
LASER USING HOLOGRAPHIC IMAGERY

Final Report

C. R. WIMBERLY



DECEMBER 31, 1979

U. S. ARMY RESEARCH OFFICE
GRANT NUMBER DAAG29-76-G-0044

UNIVERSITY OF MISSISSIPPI
MECHANICAL ENGINEERING DEPARTMENT
OXFORD, MISSISSIPPI 38677

University

APPROVED FOR PUBLIC RELEASE:
DISTRIBUTION UNLIMITED.

410 791

80 4 15 035

DATA FILE COPY

THE FINDINGS IN THIS REPORT ARE NOT TO BE
CONSTRUED AS AN OFFICIAL DEPARTMENT OF
THE ARMY POSITION, UNLESS SO DESIGNATED
BY OTHER AUTHORIZED DOCUMENTS.

Unclassified

SECURITY CLASSIFICATION OF THIS PAGE (When Data Entered)

REPORT DOCUMENTATION PAGE		READ INSTRUCTIONS BEFORE COMPLETING FORM
1. REPORT NUMBER DAAG29-76-G-004 (13224 E)	2. GOVT ACCESSION NO.	3. RECIPIENT'S CATALOG NUMBER 9
4. TITLE (and Subtitle) 6 An Investigation of Turbulent Mixing in the Chemical Laser Using Holographic Imagery. Turbulent	5. TYPE OF REPORT & PERIOD COVERED Final Report, 1 Dec 75 - 30 Nov 79	
7. AUTHOR(s) 10 C. R. Wimberly	8. CONTRACT OR GRANT NUMBER(s) DAAG29-76-G-0044 15	6. PERFORMING ORG. REPORT NUMBER
9. PERFORMING ORGANIZATION NAME AND ADDRESS Mechanical Engineering Department University of Mississippi Oxford, Mississippi 38677	10. PROGRAM ELEMENT, PROJECT, TASK AREA & WORK UNIT NUMBERS 16 IT161102BH57 06 17	11. REPORT DATE 31 Dec 79
11. CONTROLLING OFFICE NAME AND ADDRESS U. S. Army Research Office Post Office Box 12211 Research Triangle Park, NC 27709	12. NUMBER OF PAGES 89	13. SECURITY CLASS. (of this report) Unclassified
14. MONITORING AGENCY NAME & ADDRESS (if different from Controlling Office) 12 1	15a. DECLASSIFICATION/DOWNGRADING SCHEDULE NA	15. SECURITY CLASS. (of this report) Unclassified
16. DISTRIBUTION STATEMENT (of this Report) Approved for public release; distribution unlimited.	17. DISTRIBUTION STATEMENT (of the abstract entered in Block 20, if different from Report) NA 18 AF 19 13-27.1-E	
18. SUPPLEMENTARY NOTES The findings in this report are not to be construed as an official Department of the Army position, unless so designated by other authorized documents.		
19. KEY WORDS (Continue on reverse side if necessary and identify by block number) Turbulence, Holography, Laser, Chemical		
20. ABSTRACT (Continue on reverse side if necessary and identify by block number) An investigation was conducted to determine the mixing characteristics in Chemical Laser systems using a holographic flow field diagnostic network. Cold flow simulation was done using a variety of nozzles in an effort to uncover the effects of geometry, flow conditions and gas mixture combinations on the mixing of high speed parallel jets. ←		

TABLE OF CONTENTS

LIST OF APPENDIXES	ii
LIST OF FIGURES	iii
LIST OF TABLES	v
SYMBOLS	vi
I. INTRODUCTION	1
II. CHEMICAL LASER SYSTEMS	2
III. HOLOGRAPHIC SYSTEM	7
IV. COLD FLOW TEST PROGRAM	18
V. ANALYSIS	53
BIBLIOGRAPHY AND REFERENCES	56
APPENDIX A - Shadow, Schlieren and Holographic Fundamentals	62a
APPENDIX B - Density-Refractive Index Relationship	69
APPENDIX C - Computer Programs Including Subroutines	76

Accepted For	
NAME	Mr. G. L. R.
LAB. NO.	100-243
INSTRUMENT	Unknown
APPLICATION	Calibration
Date	
Date Received	
Date of Approval	
1. <input type="checkbox"/> Regular	2. <input type="checkbox"/> Special
3. <input type="checkbox"/> Regular	4. <input type="checkbox"/> Special
Initials	

A

LIST OF APPENDIXES

APPENDIX A	Shadow, Schlieren and Holographic Fundamentals	56
APPENDIX B	Density-Refractive Index Relationship	69
APPENDIX C	Computer Program Including Subroutines	76

LIST OF FIGURES

<u>Figure</u>	<u>Page</u>
1 Description of the flow processes in a supersonic diffusion HF chemical laser (Reference 3).	5
2 Plot of Current vs. Power at Photoplate for Argon laser.	29
3 Amplitude and Phase-Modulated Interference-Grating.	30
4 Recording of hologram for a plane-wave generating object (M1).	30
5 Recording of hologram of 3-d object (Stroke G.W.).	31
6 Reconstruction of Plane-Waves from hologram.	31
7 Interference pattern of a diffraction grating illuminated by a plane-wave	32
8 Spherical Wavefront Interference Pattern	32
9 Fourier Transform Reconstruction from Fourier-Transform Hologram $H(x)$. (Ref. 6).	33
10 Hologram-Recording Parameters. (Ref. 6).	33
11 A Typical Hurter-Driffield Curve for a photographic recording medium.	34
12 Variation of Reconstruction efficiency η for fixed β and E_0 values as a function of $R = I_R/I_0$. (Ref. 7).	34
13 Typical Transfer Characteristic Curve for a photographic medium (Kodak 649 F Plate). (Ref. 4).	35
14 A simple method of recording a hologram by superposition of a coherent background over a scattered field. (Ref. 4).	35
15 The laser cavity. (Ref. 4).	36
16 Possible Resonant Frequencies Centered About One Color. (Ref. 4).	36
17 The Tilted Etalon in a Laser Cavity.	36
18 Tilted Etalon Characteristic Curve. (Ref. 4).	37
19 Spatial Filtering Arrangement for Lasers. (Ref. 1).	38
20 Holographic and Gas Dynamic Facility.	39

<u>Figure</u>		<u>Page</u>
21	Reconstruction Optics and Gas Dynamics Facility.	40
22	Nozzle Relation of Design No. 1.	41
23	Nozzle Design No. 1 (dimensions in mm).	42
24	Nozzle No. 2 (from "LAMP" Program).	43
25	Nozzle No. 2 (Secondary).	45
26	Nozzle No. 2 (Primary).	46
27	Nozzle No. 3.	47
28	Nozzle No. 3 (Secondary)	48
29	Nozzle No. 3 (Primary).	49
30	Nozzle No. 4.	50
31	Shadowgraph of Mach 3 Test (Run 1).	57
32	Interferogram of Test Flow (Run 3).	57
33	Schlieren of Test Flow (Unmatched Flow - Run 5).	58
34	Schlieren of Test Flow (Matched Flow - Run 6).	58
35	Shadowgraph of Test Flow (Zero Center Flow - Run 9).	59
36	Shadowgraph of Test Flow (Matched Flow - Run 11).	59
37	Schlieren of Test Flow (Horizontal Knife Edge - Run 12).	60
38	Schlieren of Test Flow (Vertical Knife Edge - Run 14).	60
39	Shadowgraph of Test Flow (Run 15).	61
40	Schlieren of Test Flow (Run 17).	61
41.	Schlieren of Test Flow (Run 20).	62

List of Tables

<u>Table</u>		<u>Page</u>
I.	Samples of Path-Length Matching Adjustments	27
II.	Photoplate Power-Meter Readings	28
III.	Coordinates of Nozzle No. 2.	44
IV.	Test Conditions - Nozzle 4 (Secondary).	51
V.	Test Conditions - Nozzle 4 (Primary).	52

SYMBOLS

m	Mass flow rate
A	Area of nozzle cross-section
M	Mach number
N	Number of species in the mixture
M	Molecular weight
D	Nozzle throat diameter
P	Pressure
R	Gas Constant
T	Temperature
X	Coordinate along the nozzle centerline (see Fig. 6)
Y	Coordinate perpendicular to X-axis
V	Velocity in one-dimensional analysis
u	Velocity along the X-axis
v	Velocity along the Y-axis
C_p	Specific heat at constant pressure
C_v	Specific heat at constant volume
k	Specific heat ratio
f	Mass fraction
\bar{x}	Mole fraction
a	$=u_0/\mu$
ψ	Stream function
ρ	Density
μ	Viscosity
g_c	Gravitational Constant
δ_1	Boundary layer thickness defined by $u = .99u_c$
δ_2	Displacement thickness

Subscripts

- c Centerline properties
- o Stagnation conditions
- e Nozzle exit properties
- x Distance from throat along x-axis (see Fig. 6)
- m Mixture of gases
- i,j Species of gas mixture
- s Sonic conditions
- I,J See Fig. 7

Superscripts

- * Nozzle throat properties
- ' Dimensionless properties

CHAPTER I

INTRODUCTION

Of the various processes necessary to produce lasing from a chemical laser device, one of the critical processes in the H₂-F₂ continuous laser is the reactant mixing in the optical cavity. It is known that the chemical laser performance is dependent on the relative rates of excited state production, collisional deactivation, and the radiative processes. Consequently, it is clear that the mixing rate, through its influence on the production rate, plays an important role. It was the objective of the work discussed in this report to investigate experimentally the mixing process and its influence on laser performance.

Chemical laser systems, currently under investigation, involve extremely complicated interactions of chemistry, kinetics, optics and fluid dynamics. Of primary concern in the laser chemistry are the excited states of species in the laser cavities that provide the desired radiant energy. For many systems the exchange or transfer of excited states from one specie to another and the need for rapid combustion and interactions in the near field is essential for producing the desired radiation. Current applications involve the high-speed exhaust of hot combusting gases that are expanded through a two-dimensional contoured nozzle system with alternate nozzles of dissimilar gases for vibrational energy transformations. Parallel sonic and supersonic jets are currently being used to inject the chemicals into the cavity for mixing and power generation. To maximize the energy from the laser the gases must mix rapidly in the near field to provide rapid molecular and atomic diffusion of the gases. Fluid dynamic mixing in the laser cavity is the forcing agent that places the gaseous species in a position for maximum

and rapid diffusion.

The research effort described here was limited to an investigation of the fluid dynamic mixing of the gases as they enter the near field of the laser cavity, to correlate theory, test data and photographs of the mixing phenomena, and to establish the effects and sensitivity of properties on mixing of parallel supersonic streams. To this end, holographic impressions were obtained for cold flow tests and were used to reconstruct flow field views (shadowgraphs, schlierens and interferograms) for use in the evaluation and analysis of the cavity flow field.

CHAPTER II

CHEMICAL LASER SYSTEMS

Polanyi¹ presented many of the basic concepts we know today for the vibrational-rotational energy transfer of the chemical laser phenomenon. In his paper he observed that vibrational excited states have long spontaneous emission lifetimes and that for many chemical reactions the energy of reaction is converted efficiently into vibrational states. He defined the concepts of complete and partial vibrational population inversions and showed that both would occur as a result of reactions. The possibility of an exchange-reaction laser consequently existed and it was suggested to use low pressure, low temperature and fast flow to minimize collisional deactivation and thus provide a continuous chemical laser.

Kasper and Pimental² later reported on the concept of the vibrational transition laser, which works on a simple chain principle. After the production of a few Chlorine atoms by flash photolysis, the chain proceeds until all of the initially available H₂ and Cl₂ molecules have been consumed. The first step in the chain, being slightly endothermic, produces only ground-state HCl. The second step, however, being considerably exothermic produces HCl vibrational levels to about the sixth level.

The chemical formulation involving atomic fluorine and ammonia, atomic and evolution hydrogen and chlorine, fluorine and hydrogen, etc., typically used in chemical lasers was not addressed specifically in the experimental program except to simulate the molecular weight and specific tests of the products in a cold flow simulation of a continuous supersonic diffusion laser (SDL). In this chemical laser device, D₂ is used in the combustion of an HF laser, and vice versa, to prevent absorption of the laser radiation in the combustion products. Several types of nozzle/injector configurations

have provided good lasing performance, and were the basis for selecting the various nozzle configurations for the cold flow tests.

As discussed more fully by Warren³, Figure 1 shows a simplified sketch of the flow downstream of the nozzle/injector system in a combustion-heated SDL. Wedge-shaped nozzles are shown, but contoured nozzles are also used. For clearness, the sketch is for planar, or slit, nozzle geometries. Because of the small nozzle size (2 to 12 mm exit height) and generally low flow Reynolds numbers, fairly thick wall boundary layers are formed. Some systems have been operated with fully viscous nozzle flows; that is, with a significant degradation of centerline total head.³

The flows exiting from the individual nozzles and injectors are confined, except near the edges of the nozzle injector bank, by the flows from the neighboring nozzles and injectors. Thus, the main flow is nearly a constant-area process composed of a repetitive series of similar flows with short characteristic dimensions along the optical axis. Because of the high energy-release rate, the overall conservation laws require a significant average static pressure rise. This is achieved through the generation of shock waves, which originate at the nozzle lips and initially propagate into both the unreacted fluorine and H₂ streams.³

Each shock influences the flows from several adjacent nozzles while reaction and lasing are occurring. The strength of the initial shock waves and their effects on the unreacted stream properties and flow directions have been estimated through a displacement-thickness analysis and been found to provide significant perturbations to the initial undisturbed properties. Such processes have not yet been included in theoretical descriptions of a lasing flow.³

Downstream of the nozzle/injector face, the fluorine and H₂ streams

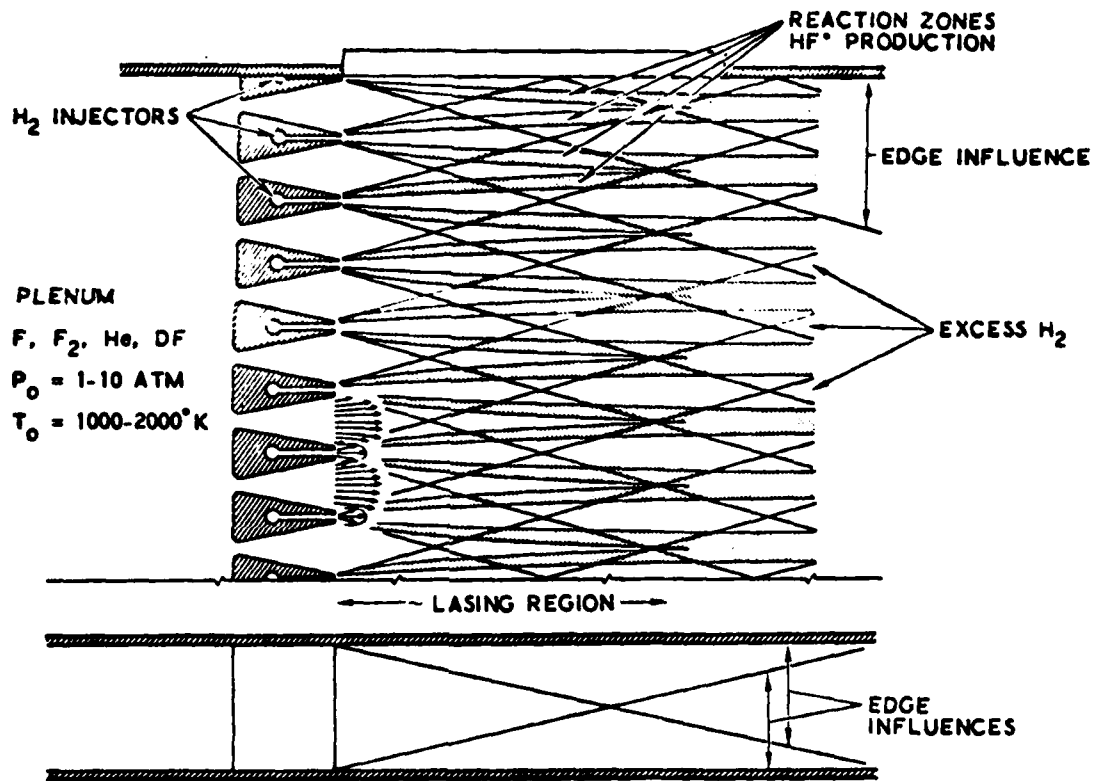


Figure 1. Description of the flow processes in a supersonic diffusion HF chemical laser (Reference 3).

diffuse into each other, and the reaction process is initiated by the F and H₂ reaction. In most SDL systems, a considerable excess of H₂ (of H₂ plus diluent) is used compared to stoichiometric, and these streams will appear to persist further downstream than do the unmixed cores of the fluorine streams. The reacting diffusion zones formed are essentially free shear layers generated by the momentum of velocity differences between the two initial streams and, to a first approximation, may be assumed to be governed by the reacting boundary-layer system of equations (away from the wave-interaction regions). The diffusion process may be laminar, transitional, or turbulent; and it is possible but not yet established, that all three processes significantly influence the flow in present SDL devices.

For a given geometry, an increase in the overall pressure level of the flow can adversely affect lasing efficiency in several ways. The diffusion zones will be thinner, at least for the laminar-mixing case, and this will delay the reaction of all the fluorine. The two-body collisional deactivation exchanges will also be faster. Such considerations have been modeled for a SDL using constant-pressure, flame-sheet, and two-vibrational-level-molecule assumptions. Scaling laws have been developed for both laminar and turbulent mixing in the reaction zones, that quantify the behaviors involved. Similar results have also been developed for a multi-vibrational-level model. Reynolds scaling can be applied to the SDL lasing process, since the important chemical production and deactivation processes are all two-body reactions and since the mixing processes are Reynolds-number dependent. The coupled reaction flow processes will scale if the product of density and length in the system is held constant. Such scaling is quite general in that it governs all of the complex processes in the flow.⁷

Chapter III

HOLOGRAPHIC SYSTEM

The holographic and reconstruction systems used in the analyses and diagnosis of the laser flow fields was a basic optics network, including three lasers, reflectors, beam splitters, collimators, and spatial filters, which collectively make up the systems. Details of the specific system is discussed in the chapter concerning the experimental program. Other information on the fundamentals of the shadow method, Schlieren technique and interferometry is presented in this chapter and in the Appendix.

Basically, the hologram of a three-dimensional scene may be considered as a window through which a precise image of the scene can be viewed. The radiation field on the viewer's side of the hologram has the same information content in either case. This radiation field, which is unique to a given object, can be extremely complex. It may be reconstructed by illuminating the hologram with a simple wave front which through the process of diffraction is converted into a more complex one.⁴ The coherent radiation field is referred to here, which originally is reflected from or passed through the object field. Any radiation generated by the object field must be excluded. Such radiation rarely meets coherence requirements and it simply adds a bias to the coherent radiation.

Holograms can be made by many methods on many types of material. The methods applied here were limited to optical holograms produced on photographic emulsions. A hologram can be made by recording the intensity of the sum of two or more waves. One of the waves must be a reproducible wave (the reference wave). The other is the modulated or object wave carrying phase and amplitude

information impressed upon it by an interest field (the object wave). The resulting recorded interference pattern, or grating, is the hologram. Except for simple cases a hologram is a complicated diffraction grating much too intricate to produce by methods usually employed to make diffraction gratings. Their reproduction is also made possible through interference of coherent waves, and subsequent recording of the interference pattern. A hologram of a point object is a grating which when illuminated by coherent light will diffract a significant portion of that light to a point in space. The grating consists of a series of concentric bright and dark rings. Holograms of more complicated objects are then understood as linear superposition of many such diffraction gratings which produce points in the image of the object.⁴

If a photographic plate is exposed to a field of fringes created by the interception of laser light, the resulting recordings form the basis for hologram classification. The developed emulsion contains surfaces of deposited silver along the bright fringes. If the developed emulsion is returned to its original recording position and illuminated by only one of the original point sources, the light reflected by the planes in the emulsion will appear to an observer to emerge from the original position. When used with the hologram, either of the point sources can be used to reconstruct an image from the other. A three-dimensional object source in general is made of many composite points. The reference source is usually a point source or collimated source of radiation which can be duplicated for the reconstruction process.⁴

In order for the fringes to be distinct, the object and reference wave-front source must be fixed relative to each other to such extent that the fringe planes will remain fixed in the emulsion during recording. The fringe planes cannot be allowed to move more than about 1/10 the separation distance between fringe planes. The criterion is most severe where motion of either source exists and will deteriorate the recording. The criterion is most easily met where motion greater than λ is tolerable. The film resolution capability must also be at least equal the fringe spacing. Again, the white light case is most severe, requiring $\lambda/2$ resolution. For green light this is in the order of 5,000 lines per millimeter, approaching the limit of the best photographic emulsions available. As the angle between the object and reference beam decreases, so does the film resolution requirement, reaching its minimum for the in-line case.

Except for the white light reflection case a hologram should be made with its normal bisecting the angle between object and reference radiation to reduce the effects of emulsion shrinkage. Emulsion shrinkage is largely normal to the plane of the emulsion. If the above criteria is met, fringe planes will lie normal to the emulsion and shrinkage will not change the fringe spacing. This effect becomes more severe for thicker emulsions. When the emulsion thickness is increased to the same order as the fringe spacing, the hologram must be illuminated by the reference wave more precisely at the same angle used in recording. This allows more than one image to be stored in a thick emulsion hologram and if different reference beam angles are used, the images can be reconstructed independently. When a thin emulsion hologram is illuminated by reference source not identically matching the original reference source used

to make the hologram, three things happen: (1) the reconstructed image position changes, (2) the reconstructed image exhibits magnification, and (3) the image becomes aberrated. Changing the radius of curvature of the reference wave causes spherical aberration. Changing its angle of illumination of the hologram causes distortion, coma, and astigmatism. Changing its wavelength causes chromatic aberration. The effects of aberrations become more serious as fringe spacing is reduced.⁴

The utility of holography ultimately depends upon the ability of an investigator to derive data from the reconstructed image. When a hologram of an extended volume of many particles is analyzed, any individual particle image is emersed in light scattered from out-of-focus images in addition to optical noise. Since coherent optical noise often has the same appearance as smaller particle images, considerable skill is sometimes required to distinguish them.

As far as film properties are concerned for holographic purposes, it has been shown that smaller particle sizes, larger particle distances from the recording, and higher resolution of the reconstructed image require higher resolution film. For every holographic recording, the effective diffraction pattern diameter is limited either by the film noise, resolution, physical size or a combination of these factors. This effective diameter and the distance of the object from the hologram define the recorded solid angle of light and, therefore, the maximum resolution in the reconstructed image. Films are available that minimize the above factors.⁴

Silver halide photographic emulsion on glass is typically used in holography. The choice of emulsion is, however, more critical for success in holography than with photography. Choosing a film with too low of resolution

for a particular problem in photography will lead to a substandard image. The same error in holography may lead to a recording with no capability to produce an image at all. The primary factors to be considered are resolution and required exposure. Other factors are concerned with noise properties, and special absorption and scattering properties.⁴

The developed hologram can be reconstructed by illuminating the hologram with laser light, preferably at or near the frequency of which the hologram was made.

Reconstructed images may first be scanned under low magnification to provide a quick examination of the volume. Portions can then be enlarged by increasing the distance from the lens to the camera and maintaining focus with the hologram. Noise from irregularities on glass surfaces in the reconstruction system usually limits useful lens magnification to about ten.

The optics network can also be used to make interferograms. The basic principles of holographic interferometry are not different from conventional interferometry. Nevertheless, it is this field that has, perhaps, been expanded more so than any other by the introduction of holography. As discussed, interferometry is the mixing of two or more coherent waves for the purpose of making measurements which are manifested in the resulting interference fringes. Holographic interferometry is merely interferometry in which some of the associated waves are stored holographically. In one class of interferometry, a comparison wave of known character is mixed with a test wave of unknown character to determine its spatial phase variation impressed thereon by a test field or object. In a second class of interferometry, two or more waves of unknown

character are mixed for the purpose of determining the spatial phase variation of the two waves. In any of these cases holography provides a storage medium for comparison waves. Typically, test waves which exist at some instant in time are stored for late recall. This provides for mixing and comparing them with comparison and test waves which are variable at will in shape, wavelength, and mixing geometry. It also provides more time for analysis of the test wave which existed, an important factor in fluid dynamic cases.

The type of holography used in this experiment was one of direct illumination where laser light is passed through a flow field test cavity and is modulated in phase by the gas density gradients. Such a beam can be recorded in a hologram, and its analysis can be carried out at a later time. This provides for a "frozen time" optical analysis of the field. Any of the conventional flow visualization methods can be performed on the reconstructed wave. These include shadowgraph, schlieren, interferometry and many other phase sensitive methods. From a single hologram made at a given instant in time, one has an almost endless choice of viewing schemes which can be employed to examine specific flow parameters.

Both the pulsed lasers and CW lasers can be used in forming the hologram, while continuous wave lasers are used for the reconstruction. The adaptation of a conventional flow visualization system for holography requires the use of a laser illuminator, and the addition of a reference beam. The hologram commonly records the wavefront converging from the second primary mirror before it reaches that focus where a knife edge was located in the conventional system.

The wavefront of interest can then be reconstructed by illuminating the hologram with the reference wavefront. This can be accomplished by

developing the exposed photographic plate, returning it to its original position, and illuminating it with only the original reference source.⁴

It is known that holographic interferometry can provide quantitative information through the density-foreign relationship. A prerequisite for this application however, is the determination of whether the anticipated refractivity change falls within the sensitivity range of the laser.

The refractive index of a fully ionized plasma is dominated by the electron refractivity, n . The fringe displacement, N , due to the substitution of plasma for vacuum, is shown below.

$$N = \int_0^L (n-1) \, dl/\lambda \quad (1)$$

Here, dl is the element of path length along a ray, L is the distance across the test area cavity, and λ is the wavelength of the laser light source. From the dispersion relation of a transverse electromagnetic wave in a cold field free plasma is

$$\kappa^2 = (w^2 c^2) / (1 - w_p^2 / w^2) \quad (2)$$

w is the angular frequency of the laser source ($w = 2 \pi c/\lambda$) and w_p is the cavity gas frequency ($w_p^2 = 4 \pi \sigma c^2/m$). Using the definition of the index of refraction $n = ck/w$, the fringe shift relations can be obtained. For the ruby laser ($\lambda = 6943\text{Å}$)

$$N = \sigma L / 3.2 \times 10^{17} \quad (3)$$

σ is the electron density in cm^{-3} . The length L is also in cm. Normal discernible fringe displacements are between 1/10 and 30 fringe per cm^5 .⁵ Details are discussed in the Appendix.

As a matter of recording, the complex amplitude of an electromagnetic wave-front possesses both magnitude $A(x)$ and phase $\phi(x)$, each of which is essential to the structure of the wavefront. The magnitude can be recorded by simply photographing the wave-front; however, the phase is invariably lost in such a process since photographic emulsions are generally sensitive only to the magnitude or absolute value of the scattered amplitude. Holographic recording, on the other hand, provides a means for a retrievable recording of the phase as well as the magnitude of the field. One method of superposing a coherent reference beam on the field striking the photographic plate is as shown in Fig. (3) wherein a plane wave illuminates a region containing a scattering object and a plane mirror, or triangular prism. The object diffracts the incident radiation to generate a field with magnitude $A(x)$ and phase $\phi(x)$ at the plate, while the prism turns the incident plane-wave through a small angle θ to form a field with a uniform magnitude A and a linear phase variation αx . α is given by the relation:⁶

$$\alpha = 2 \pi \theta \quad (4)$$

The equation above is valid for small angles θ only. Thus, the total amplitude striking the plate is:

$$A e^{i\alpha x} + A(x) e^{i\theta x} \quad (5)$$

Hence the intensity, i.e., the quantity to which the emulsion is sensitive is given by:

$$I(x) = A_0^2 + A(x)^2 + 2A_0A(x) \cos(\alpha x + \phi(x)) \quad (6)$$

As indicated, the phase of the scattered wave-front has not been lost in computing the intensity, as it would have been if the reference beam were not present. The emulsion records some power of the intensity, that is, the amplitude transmittance of the resulting photographic plate which is given by:

$$T(x) = \left[A_0^2 + A(x)^2 + 2A_0A(x) \cos[\alpha x + \phi(n)] \right]^{-\frac{r}{2}} \quad (7)$$

where r = slope of the Hurter-Drifffield curve. The Hurter-Drifffield Curve, shown in Fig. (4), relates the optical density to the exposure of the hologram for a particular photographic emulsion. The time of exposure of the hologram may be related to the intensities of the object and reference beams by the expression:

$$E = \left[I_R + I_0 + 2\sqrt{I_R I_0} \cos(Ky) \right] t \quad (8)$$

where I_R = Ref. Beam Intensity

I_0 = Object Beam Intensity

t = Exposure Time

K = Constant = f (incident angles of object and Ref. waves).

The optical density is the common logarithm of the opacity θ , where $\theta = 1/T^2$. T is the light intensity transmission, i.e.,

$$D = \log_{10} (\theta) = \log_{10} (1/T^2)$$

$$= -2 \log_{10} T \quad (9)$$

The linear portion of the H-D curve is often referred to as the range for correct tone reproduction. The slope of this curve in the linear range is the r of the developed emulsion. For a given material the value of r can be controlled by changing the type of developer and the time of development.⁷

From the theory of optical diffraction, it may be shown that the complex amplitude of the electric-field vector at a point in the image-plane of an image-forming system is the Fourier transform of the distribution of the complex amplitude of the electric-field within the image forming aperture. In other words, in order to mathematically obtain the distribution of the complex amplitude of the electric field vector at the image plane, one has to carry out a Fourier transformation for each point in the diffraction pattern.

Mathematically, the above facts may be stated as:

$$\bar{E}_p (K\alpha, K\beta) = \frac{i}{\lambda} \frac{\exp(-iKR)}{R} \iint_{\text{aperture}} \bar{E}_0 \exp [iK\Lambda(x, y)] \exp [-iK(\alpha x + \beta y)] dx dy \quad (10)$$

\bar{E}_p is the complex amplitude of the electric-field vector at a point P in the image-plane in the vicinity of the center of a quasi-spherical wave-front of radius R . α and β are the direction cosines defining the position of P as

seen from the aperture centered on the axis of the quasi-spherical wave-front, x, y are the coordinates defining the aperture $\Delta(x, y)$ the aberration of the wave-front from sphericity and $k = 2 / \lambda$ where λ is the wave-length of light used. For example, in the case of a rectangular aperture,

$$\bar{E}_p(k_x) = \frac{i}{\lambda} \frac{\exp(-ikR)}{R} \int_{-A/2}^{A/2} \exp(-ik_x x) dx \quad (11)$$

CHAPTER IV

Cold Flow Test Program

A sketch of the holographic system and gas-dynamics facility used in the study is shown in Figure 20. The components of the system are listed below:

- a) CR-5 Argon Laser (CW) (Tunable freq.) Energy is 5W at 5145 \AA .
- b) Korad KQ1000H Solid State Ruby Pulse Laser - 6943 \AA Energy 300 NW/cm²
- c) Spatial Filters XYZ - XY Traverse Stages
- d) Beam Splitters - 80-20% - AR Coated
- e) Prism Reflectors
- f) Helium Neon Alignment Laser (15 mw)
- g) 6" Spherical Concave Mirrors - 60" f1
- h) Elliptical Diagonal Mirror & 1" by 3/4" mirrors
- i) Biconvex Lenses - 2" and 4" dia., 30" f.l. and 15 " f.l.
- j) Schlieren Knife-edge XYZ Traverse Mount
- k) Film-plate Holder and Polaroid Film Holder
- l) Polaroid Land Camera.

The system was designed such that either the CW Argon laser or the pulsed Ruby laser could be used as a source without altering their position. Light from the lasers are split by the beam splitter in an 80%-20% ratio such that the reference beam is the more intense of the two. The reference beam is then reflected by the prism to the other prism on the opposite table. The object beam is reflected through prisms to the spatial filter S_1 where it is expanded to the 6" spherical mirror M_1 . Thereafter it is reflected as a collimated beam through the test section and on to spherical mirror M_2

that directs it to the photoplate. The reference beam passes through the spatial filter S_2 that expands it on to the elliptical diagonal mirror E. It then travels through the 30" f.1. lens to the photoplate to form the hologram. When the Ruby laser is used the light travels through an additional prism reflector on to the first beam-splitter and then undergoes the same process as described in the case of the Argon laser. A shutter is used to control exposure-times when the Argon laser is being used. The holographic system is set on two large tables weighted with concrete and on air cushioning provided by inflated inner tubes.

The selection of components of the holographic system was based on the type of configuration that was to be incorporated. Since the system is a transmission holographic system, the number of components is larger than a comparable reflection-type system.

The CR-5 Tunable Frequency laser was selected in order to study the light absorption characteristics of the different mixing-gases. It has a coherence length of about 10 m and can be tuned to lase at different frequencies in the blue-green range of the visible spectrum. The power output of the CR-5 is about 5 watts without the etalon and about 2 Watts with it installed. The Korad K1000QH Ruby laser is of the pulse-type and has a coherence length of about 100 cm. Its pulse-width is of the order of a 10-30 nanoseconds and operates at a single frequency of 6943 \AA with a threshold lasing value of 300 MW/cm^2 at about 5 Kilovolts.

The 45° prisms were used since metal coated reflectors would be damaged by the power of the unexpanded Ruby laser beam. Similarly, the 80-20% beam splitters for the Ruby laser beam were dielectrically coated. The spatial filtering arrangements for each of the lasers was also different. In the

case of the Argon laser the beam is first incident on a microscope objective (10X or 20X) before striking the pinhole. In the case of the Ruby laser the beam is first converged by a simple converging lens and then brought to focus at the pinhole from where it is expanded on to mirrors. An elliptical diagonal mirror was incorporated at 45° to the reference beam before passing through the bi-convex lens L_1 , in order to maintain a circular beam cross-section as it rotates through 90° and onto the photoplate. The order of flatness of all components was about a quarter wave-length of the Argon green frequency. The diameter of the 6" mirrors was selected in order to cover completely the test section windows that were 4 x 4 inches. Also their focal length of 60 inches was selected because the longer the focal length the better the sensitivity and accuracy.

The reconstruction system employed a simple 15 biconvex lens to bring the reconstructed wavefront to a focus. A Schlieren knife-edge holder with XYZ traverse positioned at the focus of the 15 lens enables Schlieren pictures to be made using a Polaroid film-pack.

In addition to the TEM_{00} mode requirement for holography, there are other important considerations necessary in laser performance. The various modes of operation of a laser are generally not coherent with each other. The lowest order mode is most widely used because the Gaussian intensity distribution is less divergent, more easily focused and is most easily used in calculations. Population inversions between several pairs of energy states allow most lasers to produce more than one frequency of light. Such a phenomenon is known as "frequency broadening", and is a hindering factor in coherent-light-imaging processes such as holography. In order to obviate this problem it was necessary to suppress other undesirable frequencies.

A technique that could be used to accomplish this involves turning the reflector inside the laser cavity. Another simple technique is the use of the tilted Fabry-Perot etalon which is inserted into the laser cavity. The transmissivity of the etalon is given by the relation⁴,

$$T_p = \left[1 + \frac{4R \sin^2}{1-R^2} (2\pi nh \cos\theta' / \lambda') \right]^{-1} \quad (12)$$

This reduces cavity efficiency at frequencies other than the etalon resonant frequencies. Figure 4 illustrates the procedure just described. The transmissivity maxima of the etalon are matched with one of the lasing frequencies by varying the angle θ' such that the peak transmission frequencies are shifted. The approximation is good when $\theta' = 0$, which was generally the case. Normally, the laser is operated at the second peak power shown in Figure 4 to realize full suppression of undesired modes.

For satisfactory performance of the optics system the first criterion was a vibration-free mounting of components. This was accomplished by fastening the components to basemounts with rigid 3/4" brass rods at the minimum height necessary. The axis of the Ruby laser was 6.688" from the table surface. All optical components such as mirrors, lenses, beam-splitters, etc. were mounted with their axis of symmetry at this height. The tables were mounted with their tops resting on air cushions provided by inflated inner tubes. The pinholes in the spatial filters were critical to provide proper alignment and diffraction. Intensity of the expanded beam was found to be nonuniform on occasions and in some cases insufficient at the photoplate. This was remedied by using pinholes of 18 to 23 microns in the object and reference beams. It was found that the quality of the beam greatly improved with an increase in the pinhole diameter.

The matching of path lengths prior to running of tests was carried out by individually fixing the distances between various components. Certain values were automatically fixed by optical constraints, e.g. the distance between the pinhole from spatial-filter S_1 to the collimating spherical mirror was fixed by the focal length of the mirror since the pinhole is required to be located at the focus for perfect collimation after reflection. Once the position of S_1 and M_1 were fixed (assuming that M_1 is centered along the axis of the test-section) the angle between the reflected object beam and its direction before reflection (ϕ_1) was also fixed. Thereafter the angle ϕ_2 between the object beam directions prior to and after reflection of spherical mirror M_2 was made equal to ϕ_1 in order to ensure that the object beam was incident on the photoplate parallel to its direction prior to striking collimating mirror M_1 . The orientation of the photoplate was also adjusted so that it normally bisected the angles between the object and reference beams at the plate. These details are indicated in Figure 18. By positioning the lasers and reflectors, the paths of the reference and object beam were adjusted to be equal.

To properly expose the plate an illumination of 10 ergs/cm^2 for a shutter exposure of 1 second for the AGFA 10 E56 film was required. A correlation was obtained for photoplate-power values at various values of laser-current. On measuring the losses in intensity through various components of the system it was noted that the prisms transmitted almost 99% of the light while the mirrors transferred nearly 100% of the incident intensity. However, it was observed that the distance between the spatial filter S_2 and the elliptical diagonal mirror was significant in that it determined the amount of the light intensity in the reference beam that actually reached the photoplate

via the elliptical diagonal mirror. The distance between the two was adjusted such that a maximum possible portion of the expanded reference beam would be incident on the elliptic diagonal mirror and hence onto the photoplate. The same occurred with regard to the distances between the elliptical diagonal mirror and lens L_1 , and L_2 , and the photoplate. An alternate arrangement of switching the position of the spatial filter S_2 and the photoplate was also tried successfully to improve the intensity. These alterations are indicated in Figures 22, 23, 24, and 25.

The alignment of the Argon and Ruby lasers were a critical and time-consuming task. The height of the Ruby laser was selected as the standard beam height and the Argon laser was elevated to that height. Alignment of the Argon laser was performed by adjusting the heights of various components in the optics. The CW Argon beam was convenient to use to align that system, while for the Ruby laser a CW helium-neon laser was positioned alongside it (shown in Figures 19, 20) where the beam was directed along the axis of the Ruby laser until it was incident on the beam splitter and thence to the optical set up for the Ruby laser. An autocollimator was also used to line up the individual components of the Ruby laser such as the laser head, Q-switch, etalon, rear reflector, etc.) prior to lining it up with the optics proper.

In order to test the stability of the system a Michelson's interferometer configuration (Fig. 21) was set up utilizing the Argon laser and the beam-splitters of the current system. The stability of the system was checked by the movement of the interference fringes when the system was slightly disturbed. It was noted that the system was extremely stable since the number of fringes moving across the field was negligible. However,

the system was not entirely insensitive to movement as the table tops were not rigid but were freely supported by the inflated tubes underneath them. Effects of a hot air draft from the laser power supply was also indicative of the sensitivity. The power supply had to be reoriented with its air-draft facing away from the system. On observing the object beam on the exit-side of the test section it was observed that oblique fringes were present across the square cross-section. These may have been caused by interference due to slightly non-parallel test-section windows, and/or interference due to asymmetry between the test-section axis and beam-axis. Adjustment of the test-section windows produced a slight improvement in the beam quality on the exit-side of the test-section.

Based on readings of photoplate illumination at various laser-current values obtained from the experiment, (Figure 6) and a value of 10 ergs/cm^2 required for an exposure, the shutter speed for the Argon laser for the various tests were determined. The beam diameter in each case was assumed to be 4". The times for developing and fixing the films were about 5 minutes each. Developing and fixing times were varied for double-exposure tests, depending on the extents of exposure. The final image is obtained by reconstructing the flow field from the hologram where the quality and efficiency of reconstruction is extremely important!

The efficiency of reconstruction n is given by

$$n = \frac{BE_0^2 M^2}{4} = \frac{\text{Reconstructed wavefront intensity}}{\text{Reference beam intensity}} \quad (13)$$

where $M = \frac{4R}{(1+R)^2}$ (14)

$$R = I_R/I_o = \frac{\text{Reference beam intensity}}{\text{Object beam intensity}}$$

$$E_o = \text{dc exposure term} = (I_R + I_o)t_{\text{exp time}}$$

β = slope of transfer characteristic curve (plot of transmission of hologram vs. exposure)

It may be seen that for a fixed E_o

$$n \propto \frac{R}{(1+R)^2}$$

which indicates that for a low value of R , the value of the reconstruction efficiency is high. However a low value of R also increases the probability of strong higher order diffractions that may severely degrade the reconstructed image. As a compromise between efficiency and image quality the value of R was chosen to be approximately 3 for most tests. Experimentally, it was found that the angle between the object and reference beams significantly influenced the resolution of the holograms. An angle of 10 degrees was finally chosen for the best resolution. Also, as the angle between the reference and object beams were increased, the chances of spurious reflections was reduced. It was noted that the image quality of the hologram was very sensitive to its alignment with respect to the reference beam. A slight rotation about a horizontal or vertical axis was found to cause noticeable changes in the clarity of images which were near the diffraction limits. Shutter exposure for the reconstruction using the Polaroid film-pack was found to be optimum at about 3-10 msec.

Shown in Table I is a compilation of results obtained from various tests. The aim of these tests was to establish the credibility of the system. Three

types of tests were performed:

- a) Object-Reflection Holograms
- b) Gas Flow Tests
- c) Flame-induced density gradient tests

Object Reflection Holograms The procedure followed was to remove the mirror M_2 and replace it with the desired object for record. In most cases both the object and reference beams were used. In one case only the object beam was used to form the hologram by placing the object in front of the mirror M_2 and blocking off the reference beam while exposing the plate. In another instance the reference and object beams were switched and distances between objects and photoplate were varied.

Flame-Induced Density Gradient Tests These tests were made with a flame that was held up in front of the test section. Using a double exposure, holograms were made and the reconstructions obtained provided high quality interferograms of the flow around the flame.

Gas-Flow Tests The primary gas flow tests used Nitrogen and Helium as the two non-reacting mixing constituents. Tests showed poor quality reconstructions partly caused by a temporary laser malfunction but also because of an extensive amount of spurious reflections from prisms, the test section, and beam splitters. Blocking off these increased the quality of the holograms.

TABLE I
SAMPLES OF PATH-LENGTH MATCHING ADJUSTMENTS

Path	OBJECT BEAM (Inches)			REFERENCE BEAM (Inches)			
	I	II	III	Path	I	II	III
Beam Splitter Prism I	27	9	9	Beam Splitter Prism III	9	6	6
Prism I to Prism II	10.5	10.5	10.5	Prism III to Prism IV	159	156	109.50
Prism II to M1	90	18	18	Prism IV Elliptic Mirror	36	30	32
M1 to M2	207	108.75	110.75	Elliptic Mirror Plate	54	72	26.25
M2 to Plate	42	24.25	24.25		-	-	-
TOTAL PATH	376	170.25		TOTAL PATH	258	264	170.25

Note: 1. Distance between spatial filter S1 and M1 = 60" for 6" mirrors
 = 45" for 4" mirrors

2. Distance of mirror EDM from L1 = 30" = f.1.

3. Distance of L2 from knife edge positioner = 15" = f.1.

TABLE II
PHOTOPLATE POWER-METER READINGS
(WITH PLEXIGLASS TEST SECTION WINDOWS)

S. No.	Laser Current (Amps)	Ref. Beam (watts)		Measuring Meter Insensitive to Changes in Power	TOTAL Ref. + Obj. Beam (watts)	
		Ref.	Obj.		Ref.	Obj.
1.	12	.01			.012	.014
2.	15	.01			.012	.014
3.	18	.012			.014	.014
4.	21	.014			.016	.015
5.	24	.015			.017	.016
6.	27	.02			.021	.019
7.	28	--				
8.	30	--	0.005			.021
						.020

Inferences: Power meter either insensitive to small power changes or was malfunctionary.

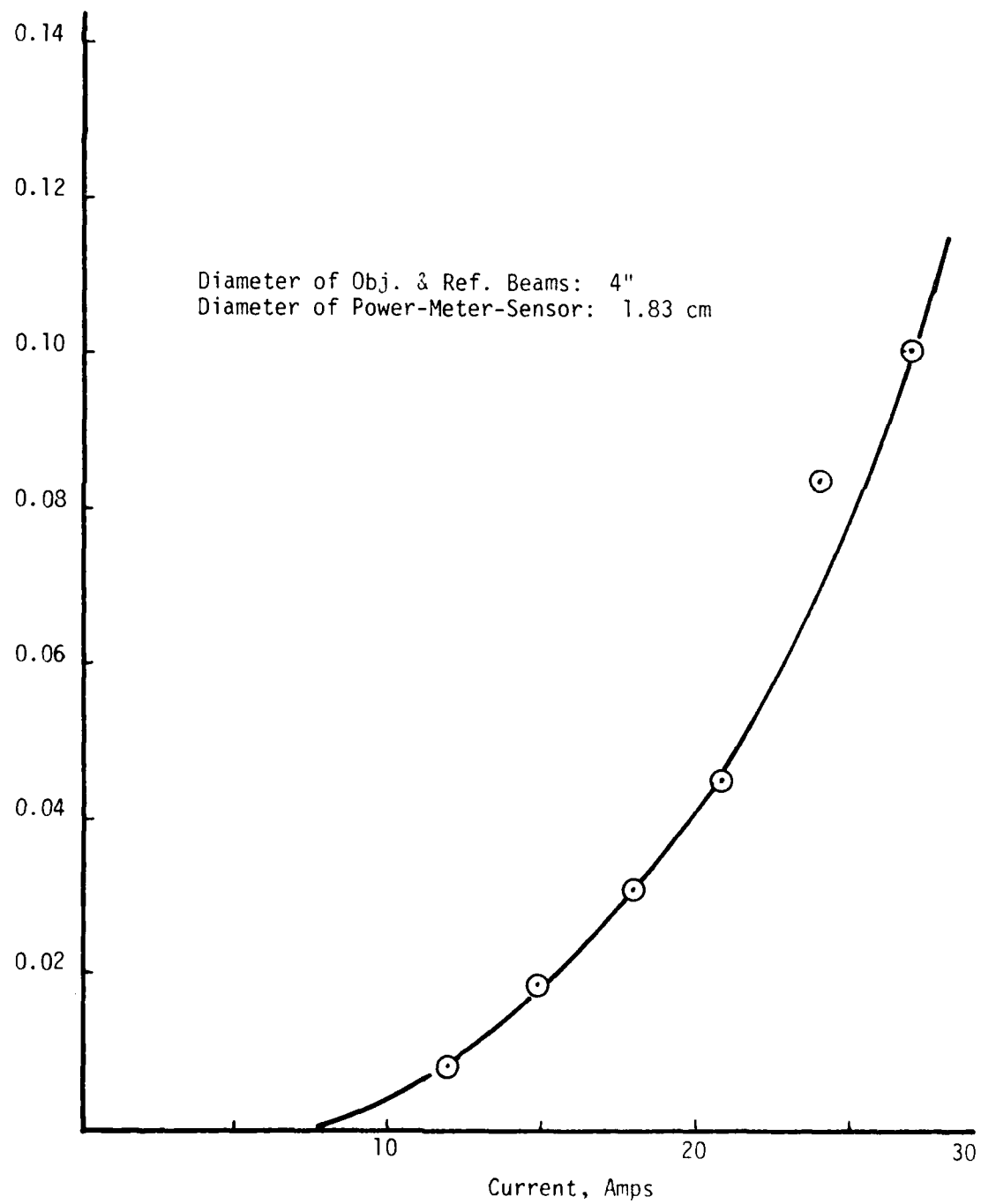


Figure 2. Plot of Current Vs. Power at Photoplate for Argon Laser.

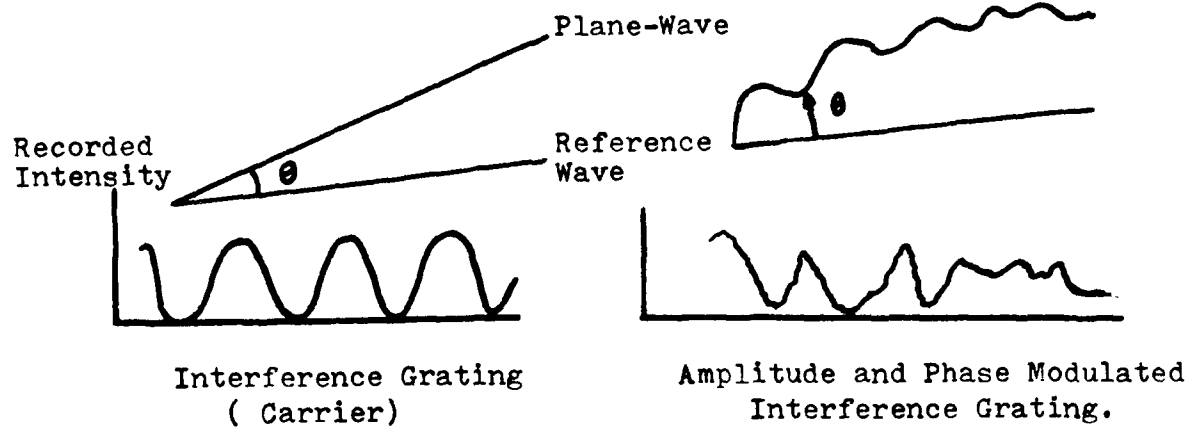


FIG. 3 . Amplitude and Phase-Modulated Interference-Grating.

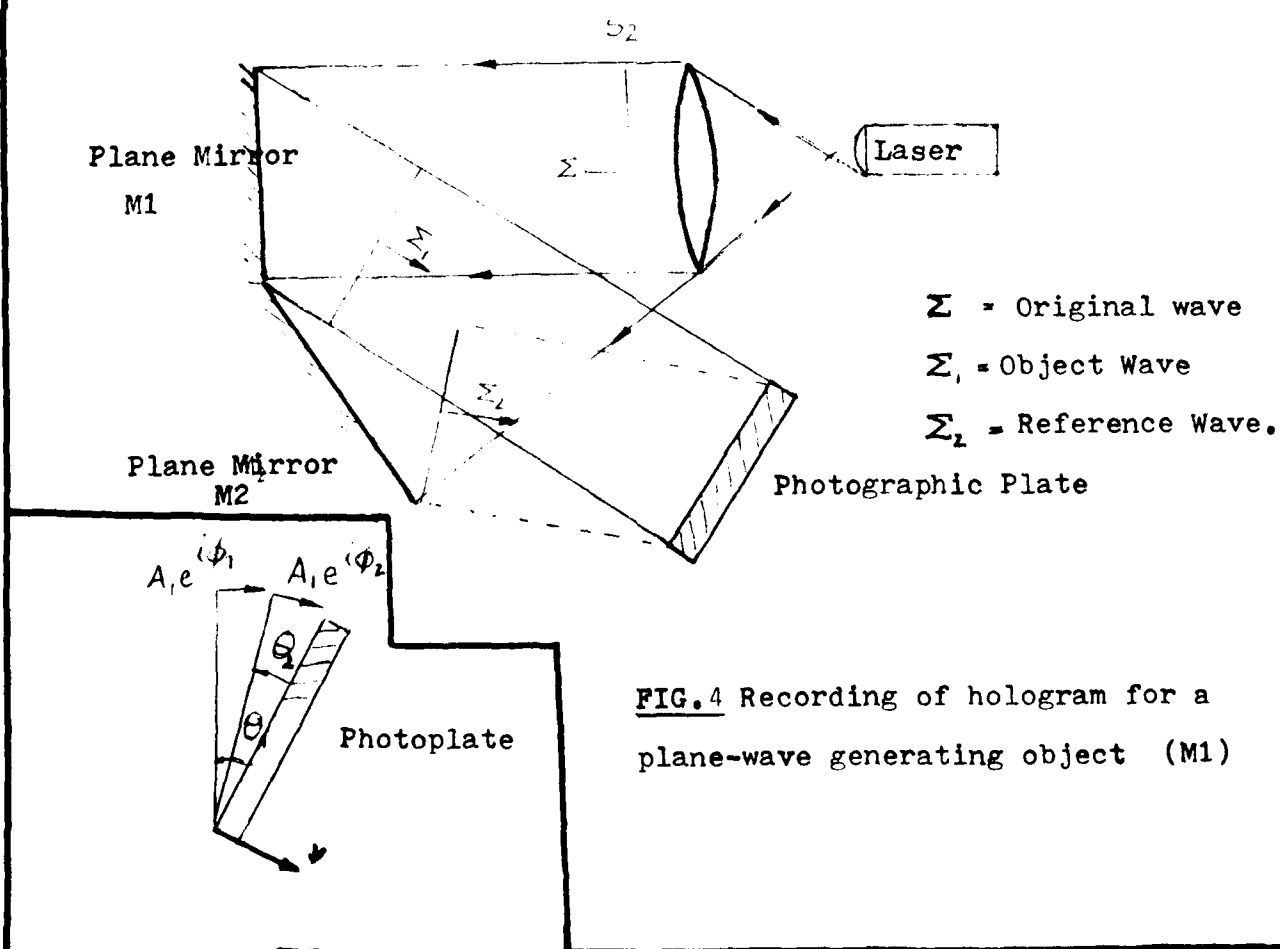


FIG. 5. Recording of hologram of 3-d object (Stroke G.W.)

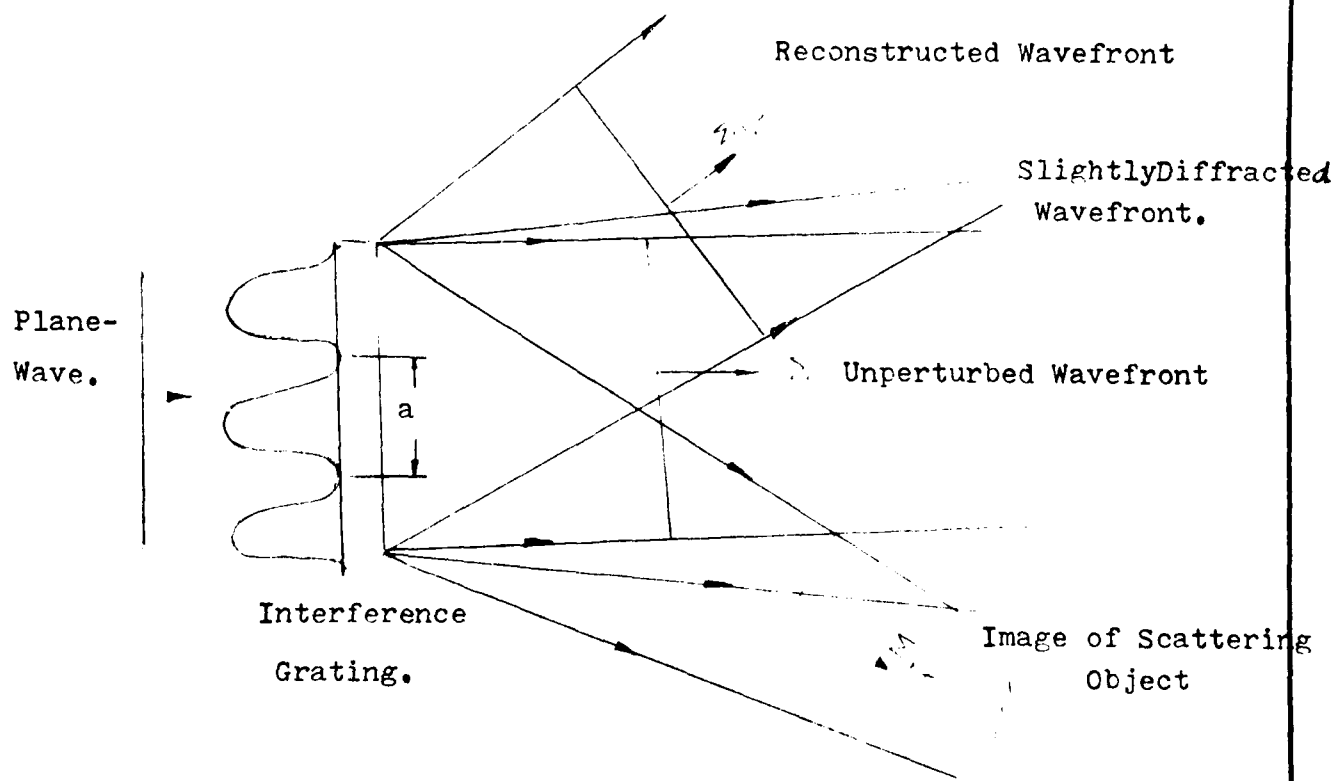
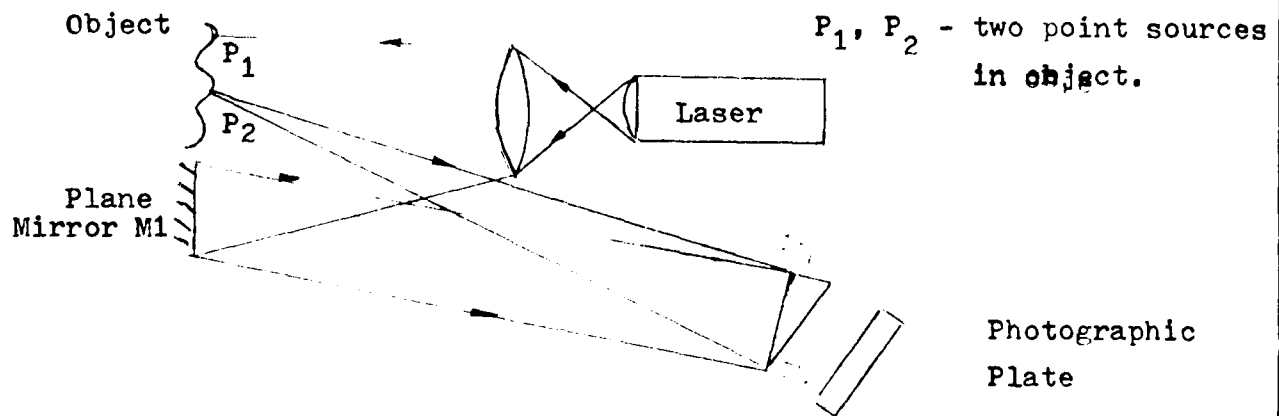


FIG. 6. Reconstruction of Plane-Waves from hologram

FIG. 7. Interference pattern of a diffraction grating
illuminated by a plane-wave

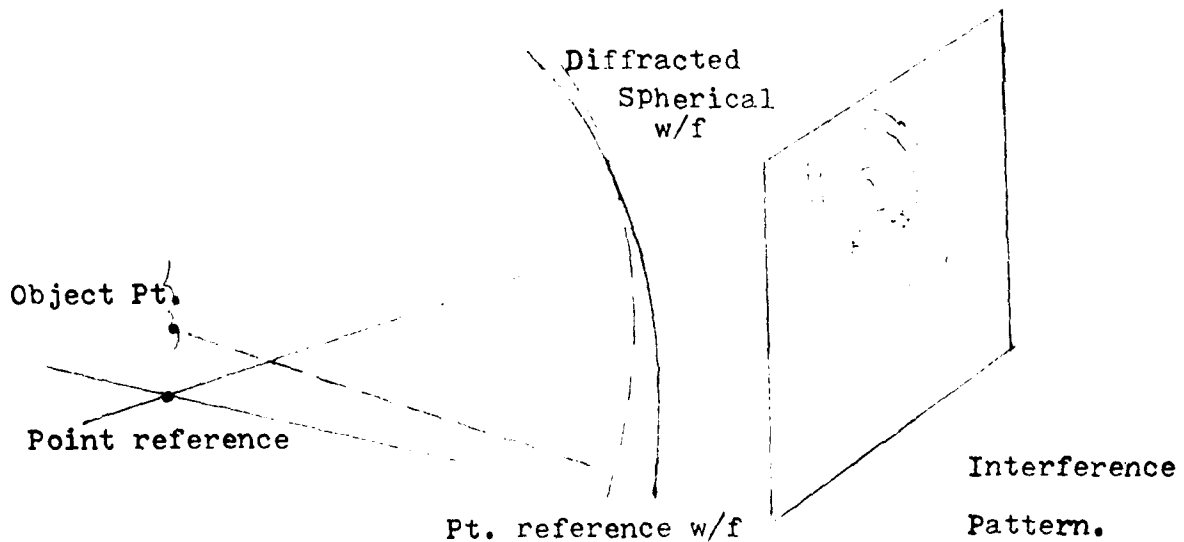
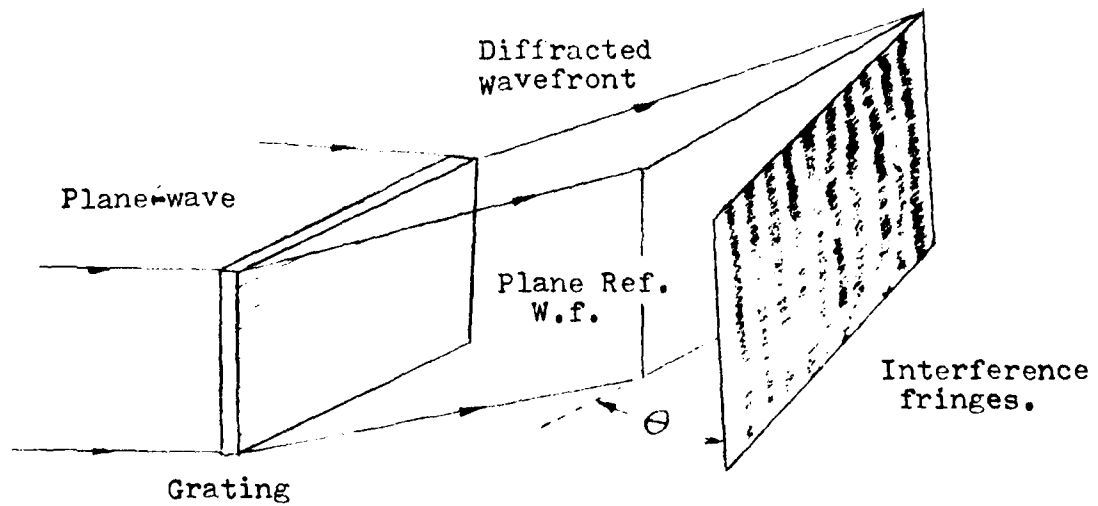


FIG. 8. Spherical Wavefront Interference Pattern

FIG. 9. Fourier Transform Reconstruction from Fourier-Transform Hologram $H(x)$. (Ref. 6)

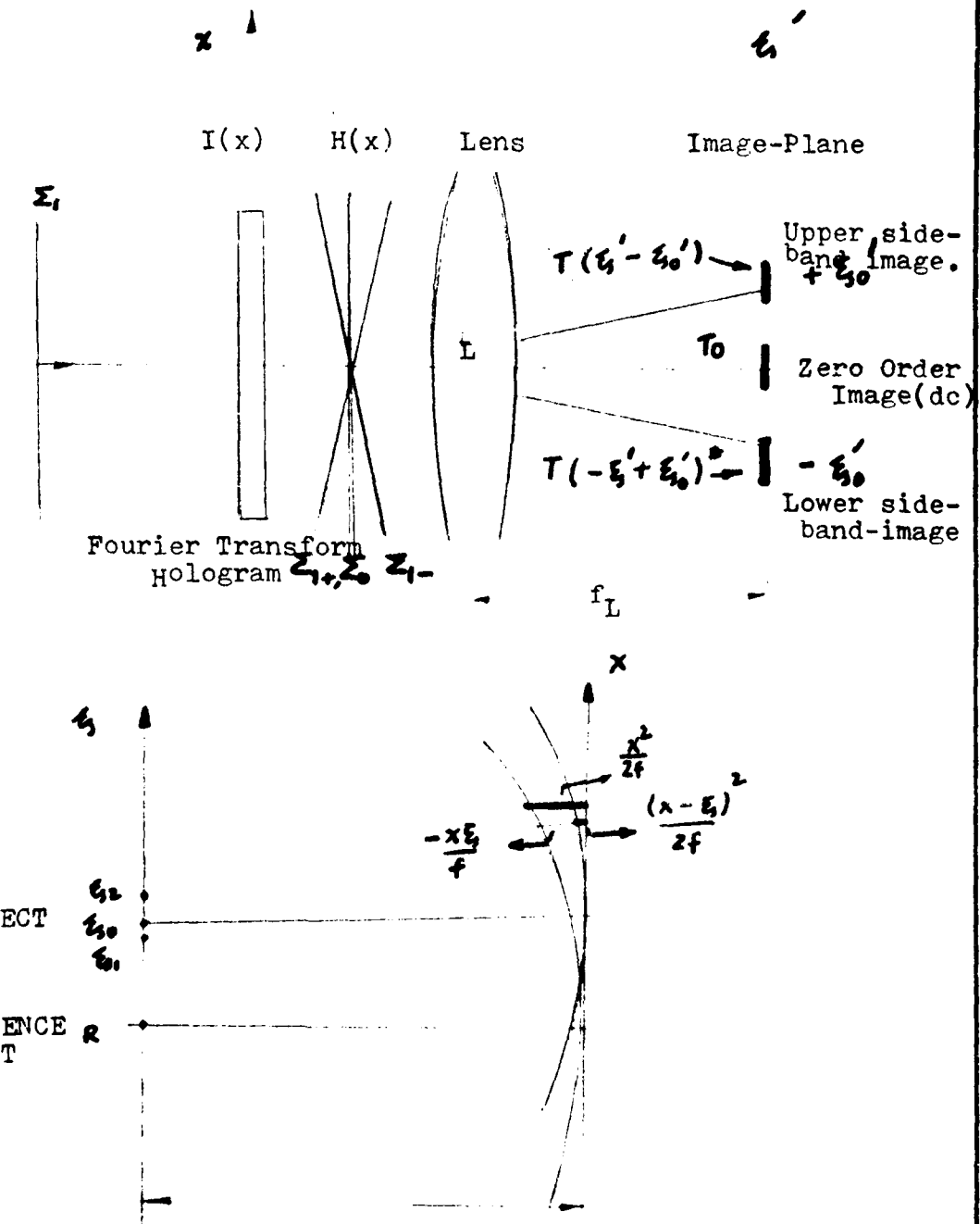


FIG. 10 Hologram- Recording Parameters. (Ref. 6)

FIG. 11. A Typical Hurter-Drifffield Curve for a photographic recording medium.
(Ref: 7)

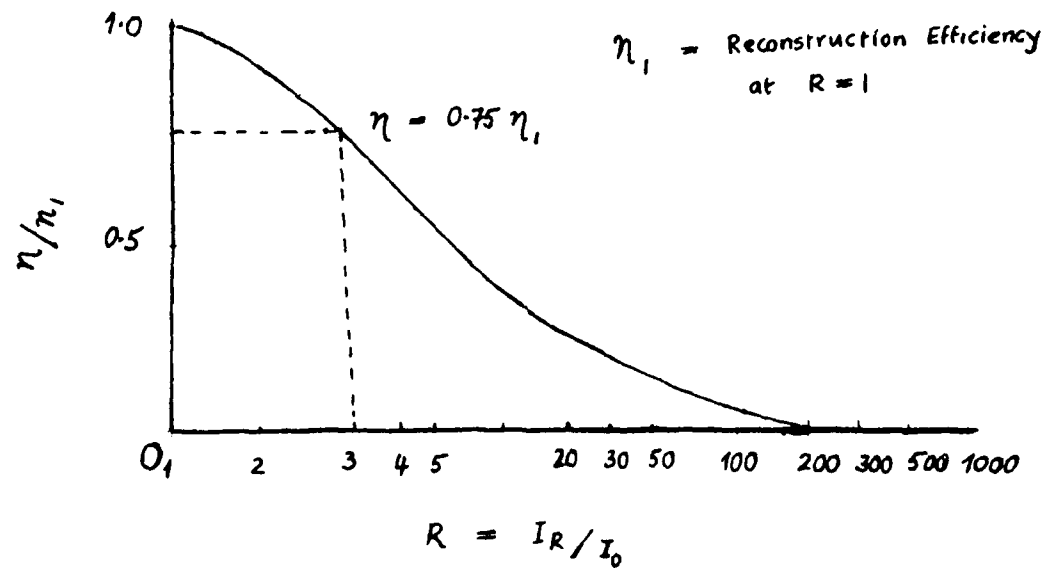
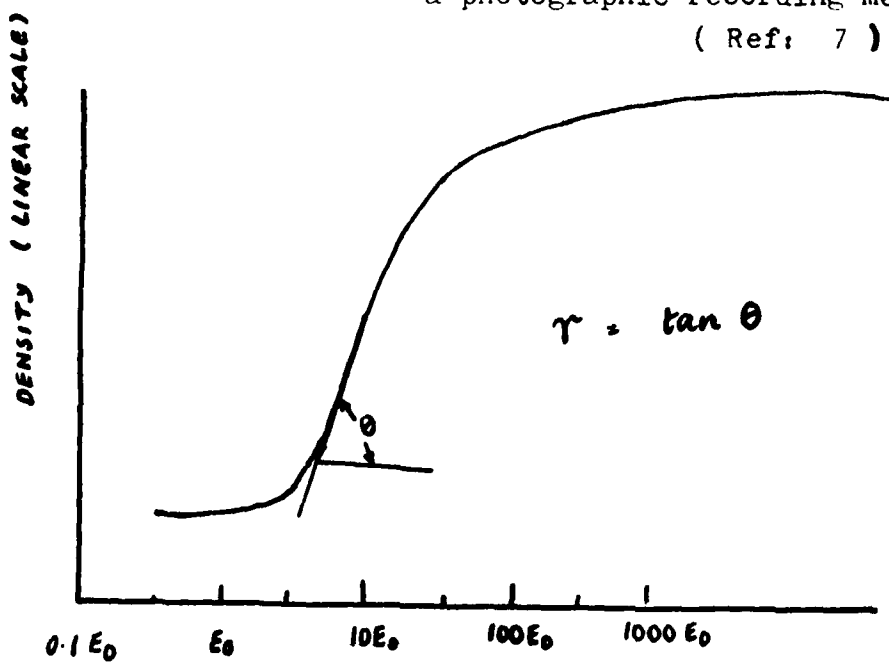


FIG. 12. Variation of Reconstruction efficiency η for fixed β and E_0 values as a function of $R = I_R/I_0$
(Ref. 7)

FIG. 13. Typical Transfer Characteristic
Curve for a photographic medium
(Kodak 649 F Plate) (Ref. 4).

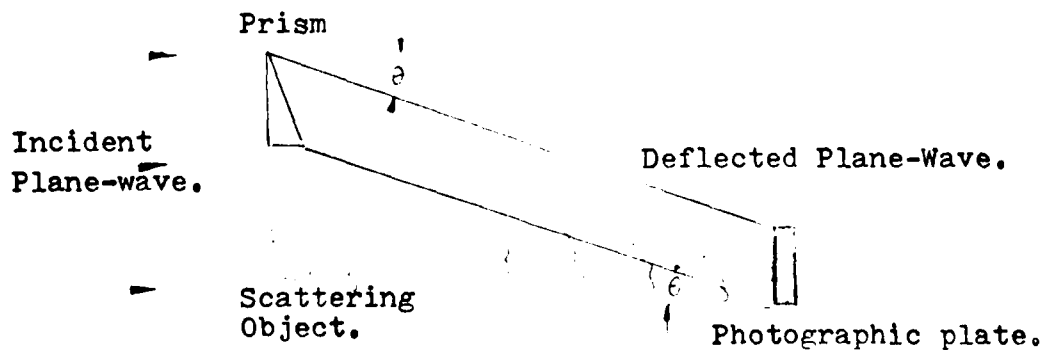
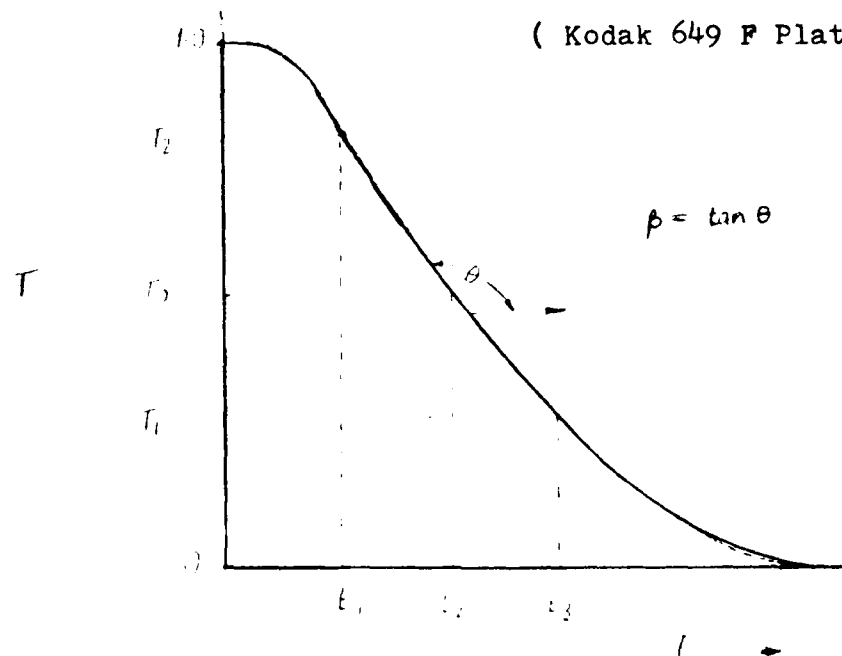


FIG. 14. A simple method of recording a hologram by
superposition of a coherent background over
a scattered field. (Ref. 4)

FIG. 15. The laser Cavity (Ref. 4).

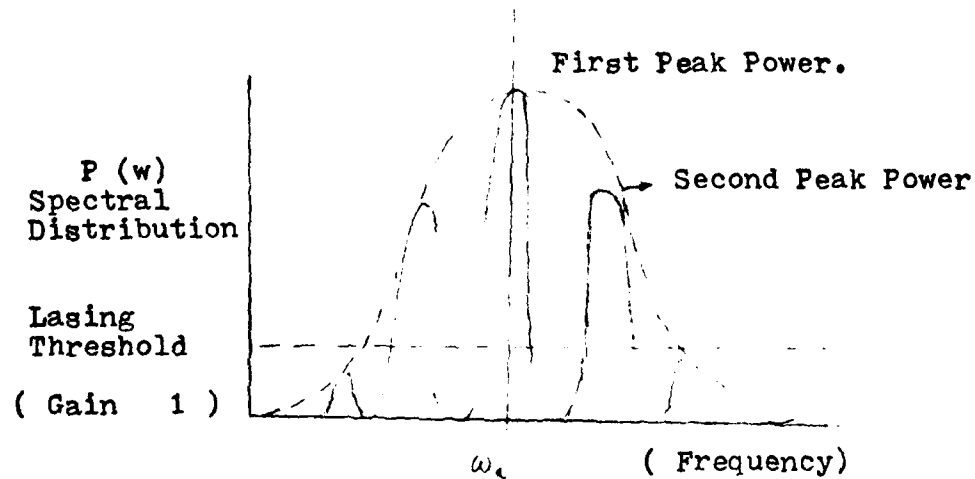
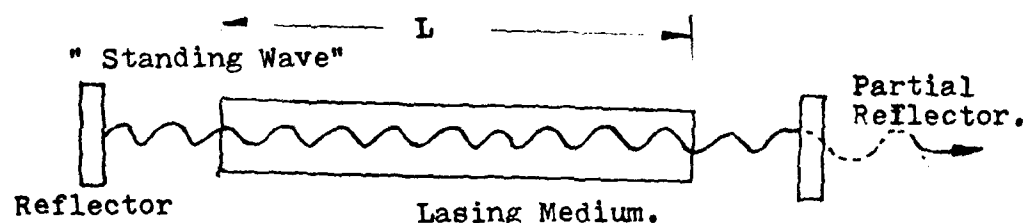
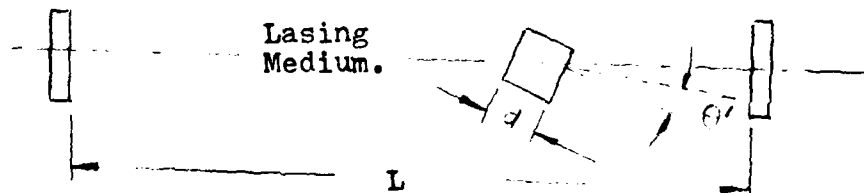


FIG. 16. Possible Resonant Frequencies Centered about one Colour (Ref. 4).

FIG. 17. The tilted etalon in a Laser Cavity.
(Ref. 4).

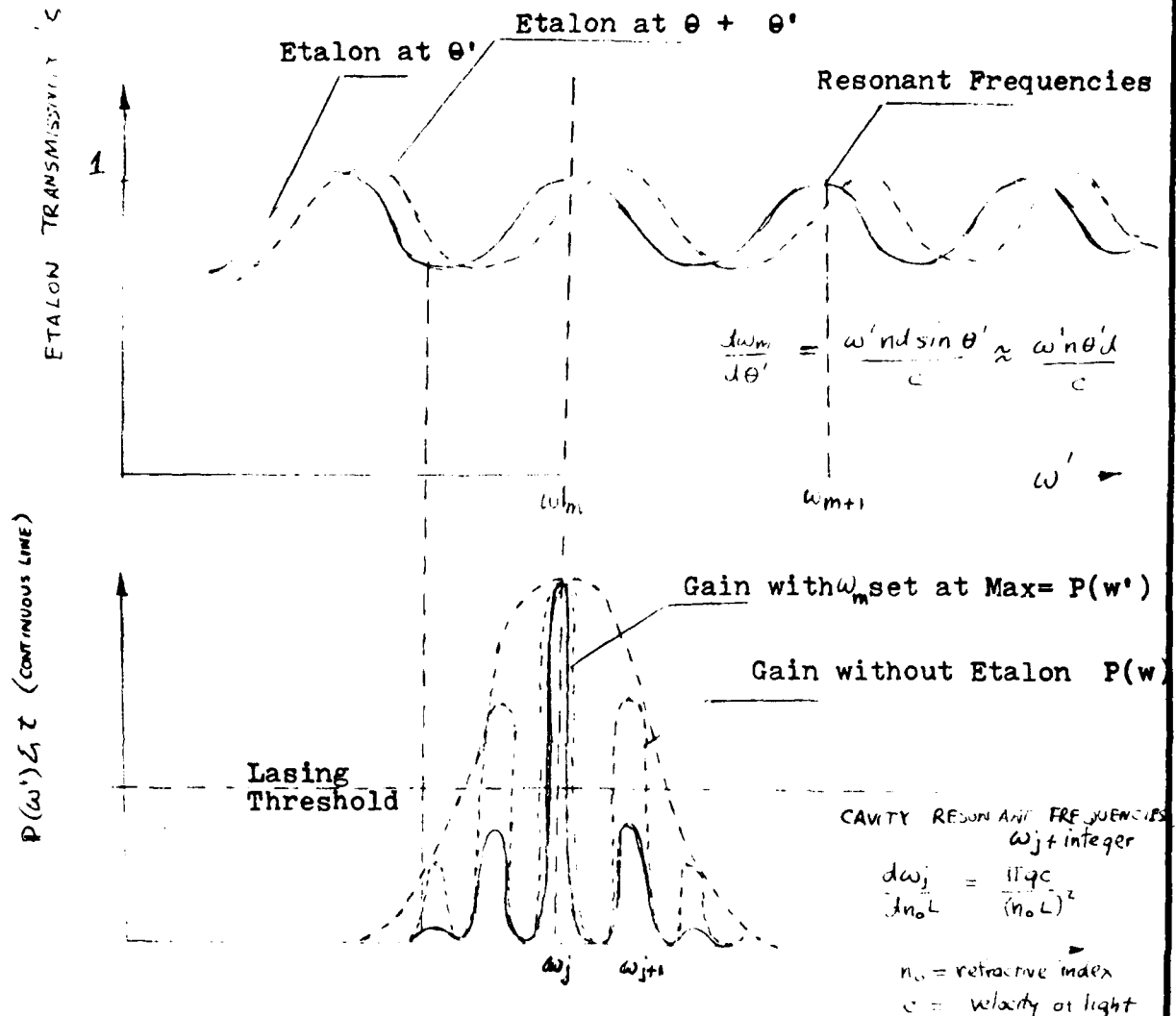
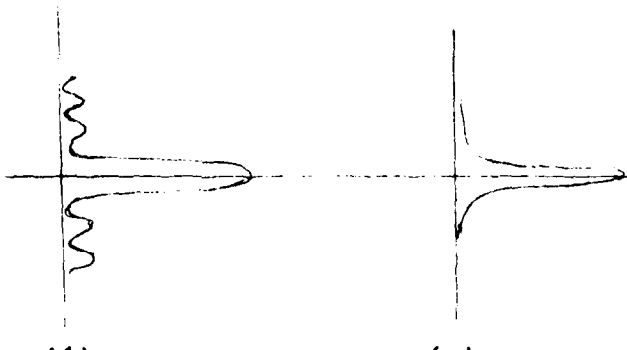
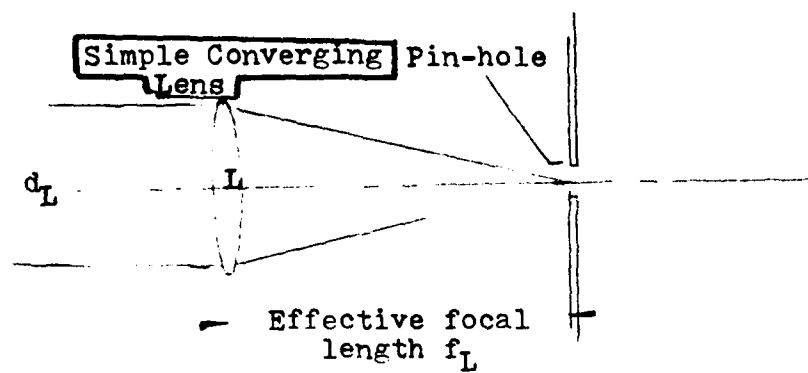


FIG. 18. Tilted Etalon Characteristic Curve. (Ref. 4

Note : "At non-resonant frequencies of etalon losses are introduced. Lasing action becomes frequency dependent. Proper selection and adjustment of etalon (e.g. tilting) sharpens the resonance curve, thus tuning laser to single-frequency mode. Tilting an etalon by more than a fraction of a milliradian causes severe losses even at resonance." (Ref. 4)

FIG. 19. Spatial Filtering Arrangement for Lasers. (Ref (1)).



Intensity Distribution at
A for Uniform Input

Intensity Distbn. at
A for Gaussian Input

Note : In the case of the Argon laser the simple lens L is replaced by a compound -lens system, usually a microscope objective of 20 X or 10 X.

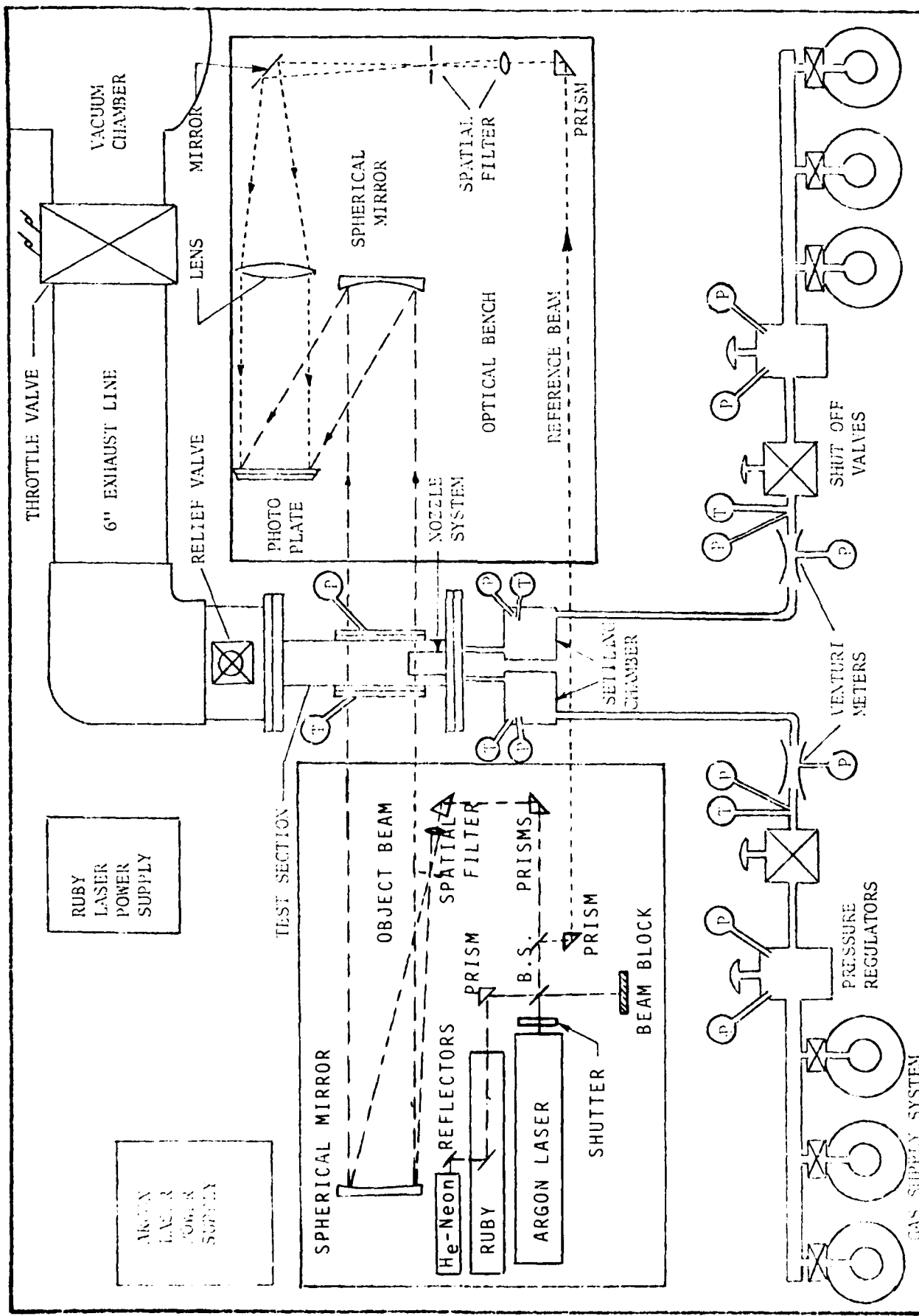


FIGURE 20: HOLOGRAPHIC AND GAS DYNAMIC FACILITY

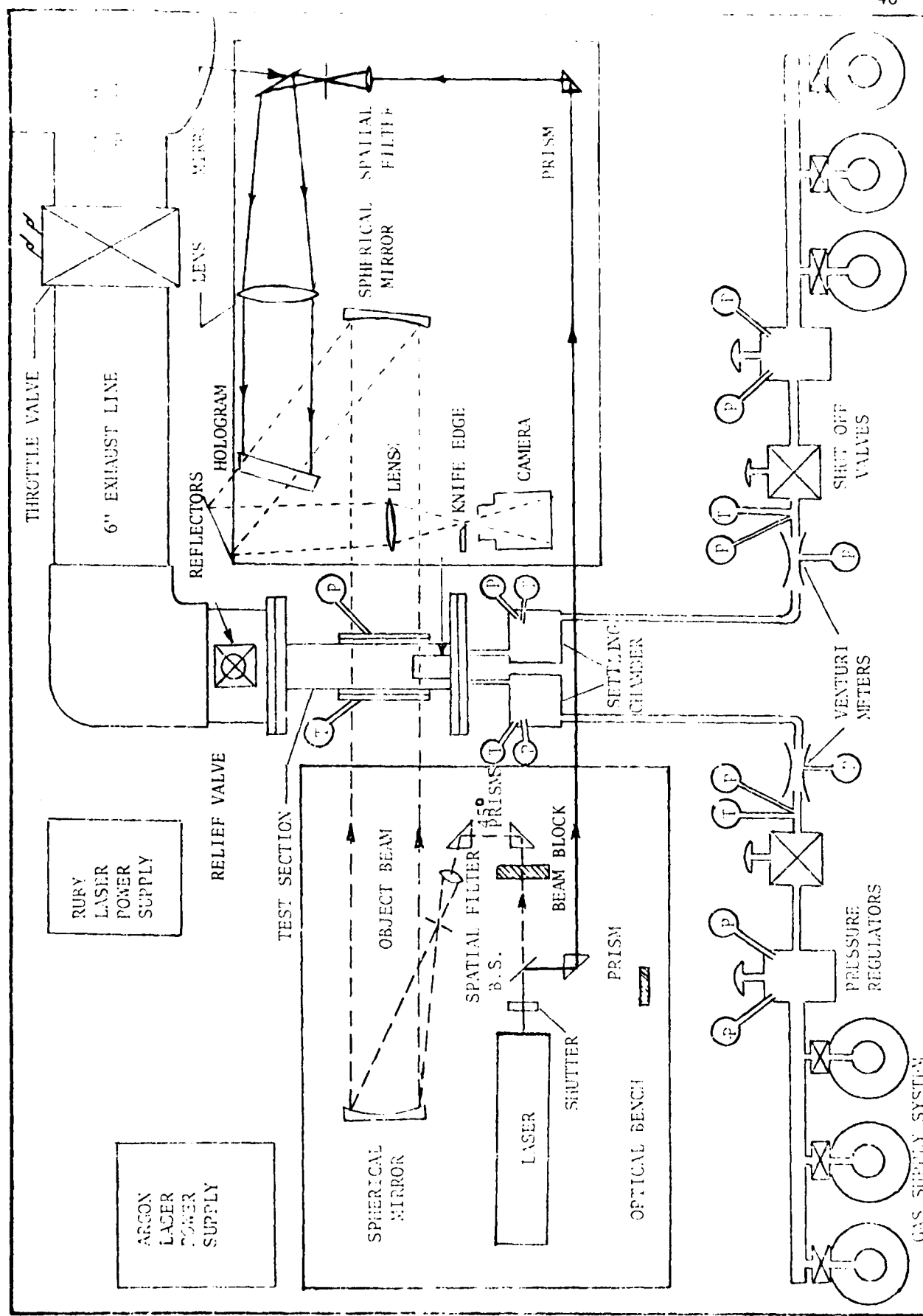
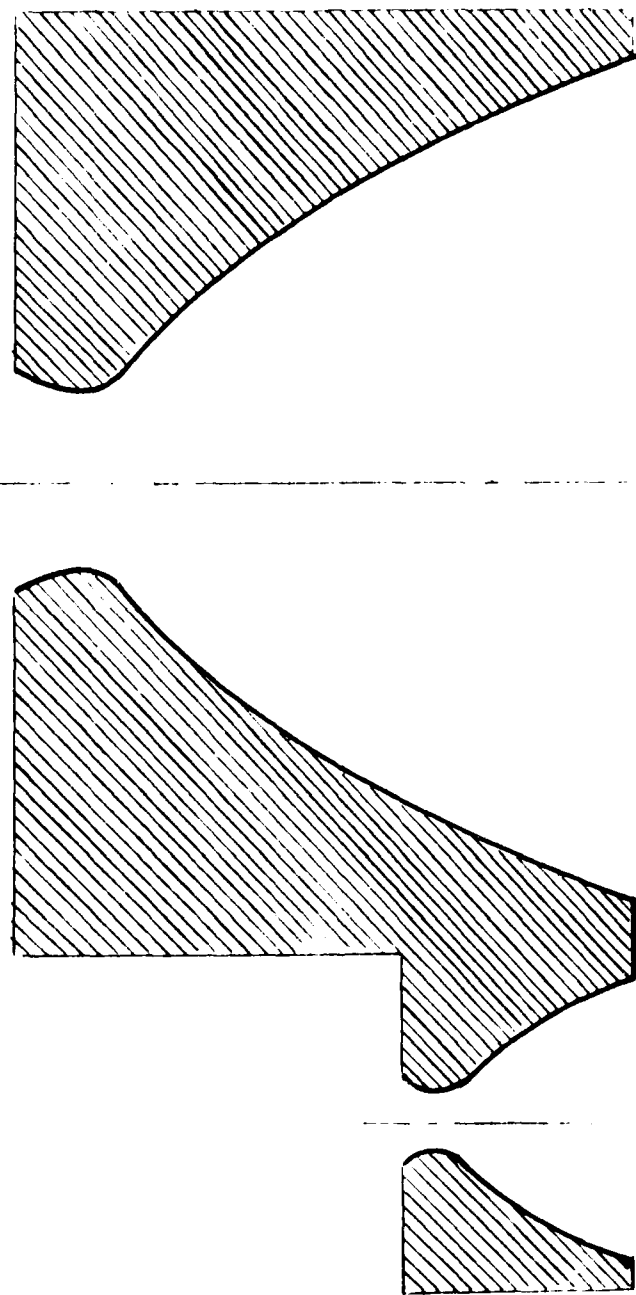


Figure 21. RECONSTRUCTION OPTICS AND GAS DYNAMICS FACILITY



SCALE: 4 TINTS

Figure 22. Nozzle Relation of Design No. 1.

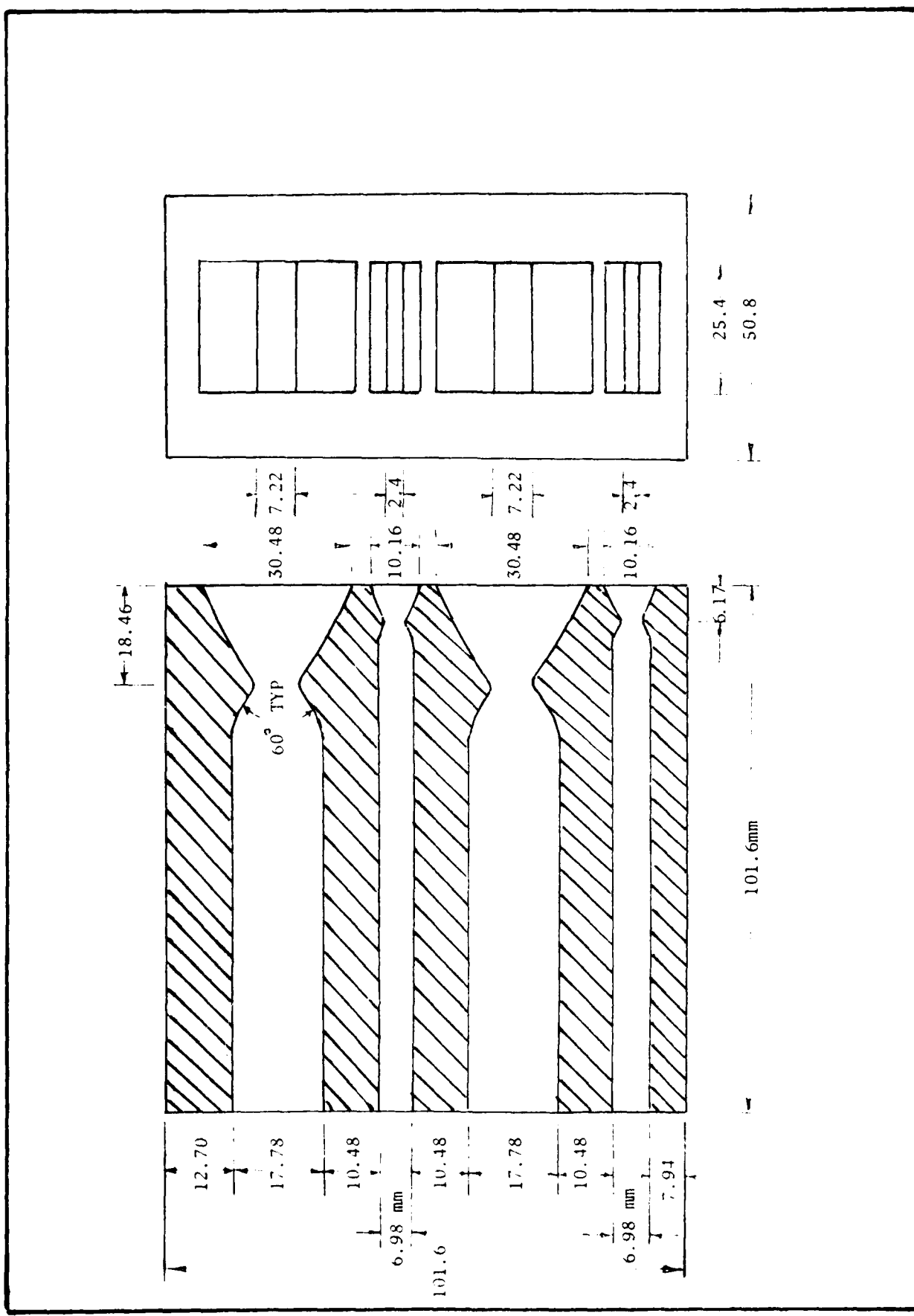


Figure 23. Nozzle Design No. 1 (dimensions in mm)

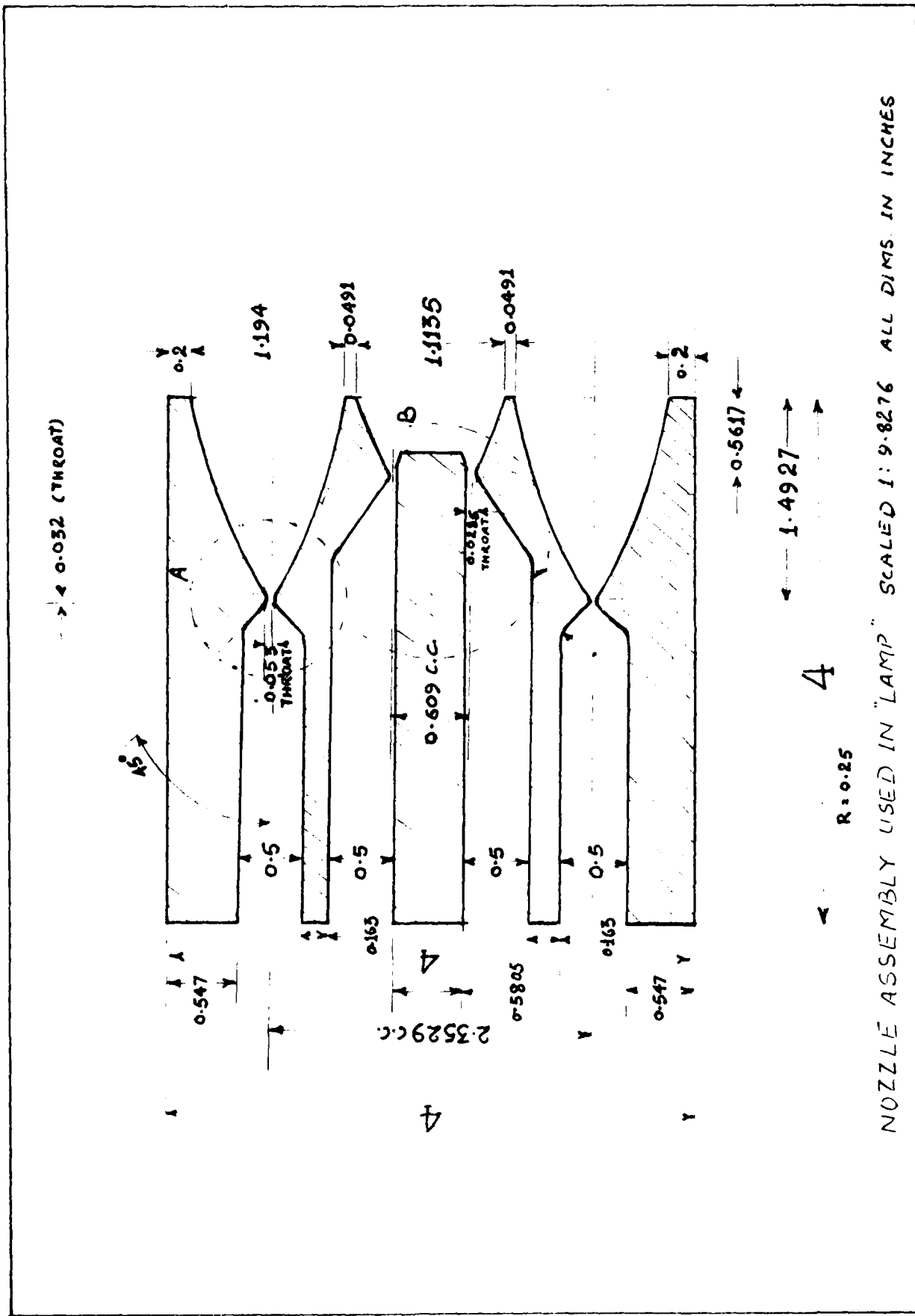


Figure 24. Nozzle No. 2 (from "LAMP" Program).

Table III. Coordinates of Nozzle No. 2.

PRIMARY NOZZLE

Station No.	X INCHES	Y INCHES
1	0.000	0.000
2	0.383	0.0295
3	0.0962	0.0692
4	0.2092	0.1321
5	0.3967	0.217
6	0.6157	0.3015
7	0.8543	0.3825
8	1.019	0.4335
9	1.2265	0.4969
10	1.493	0.5705

SECONDARY NOZZLE

Station No.	X INCHES	Y INCHES
1	0.000	0.000
2	0.05	0.0388
3	0.098	0.0703
4	0.1463	0.098
5	0.2445	0.1428
6	0.3417	0.1798
7	0.4399	0.2216
8	0.5617	0.2455

COORD. SYSTEM FOR NOZZLES WITH 0.0 AT CENTRE OF EACH

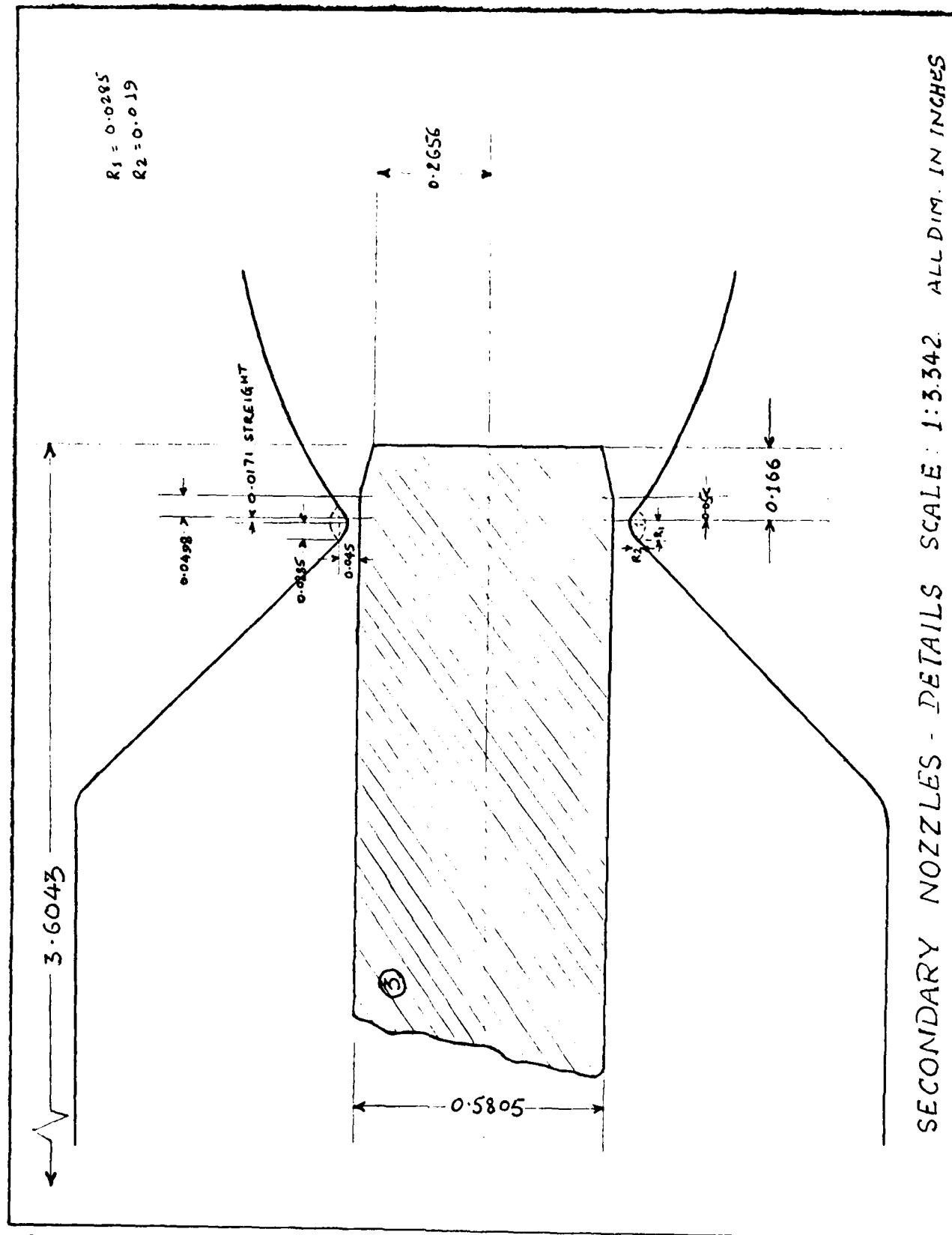


Figure 25. Nozzle No. 2 (Secondary).

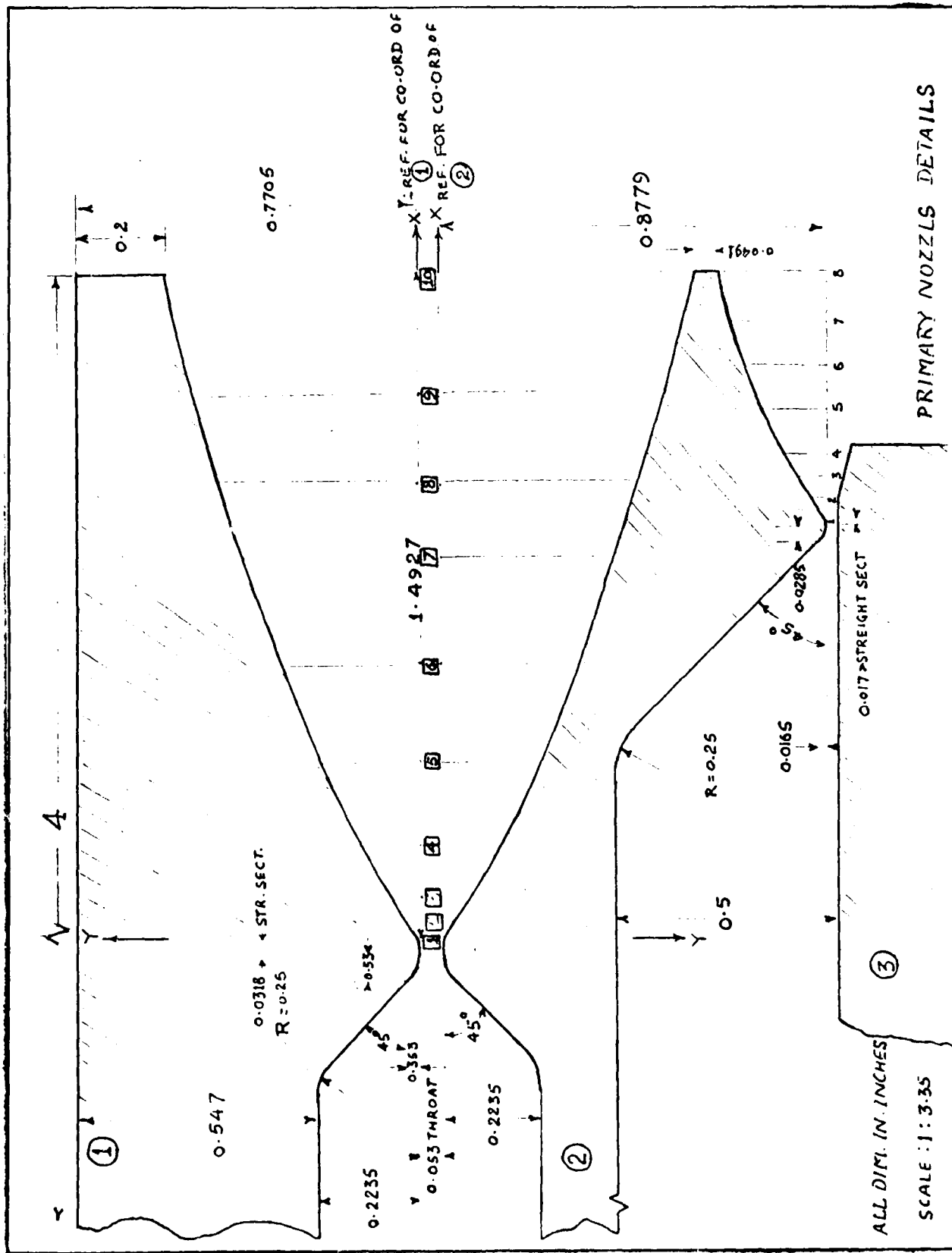


Figure 26. Nozzle No. 2 (Primary)

NOZZLE - C1 V SCALED 1:5.538 ASSEMBLY ALL DIMN. IN INCHES

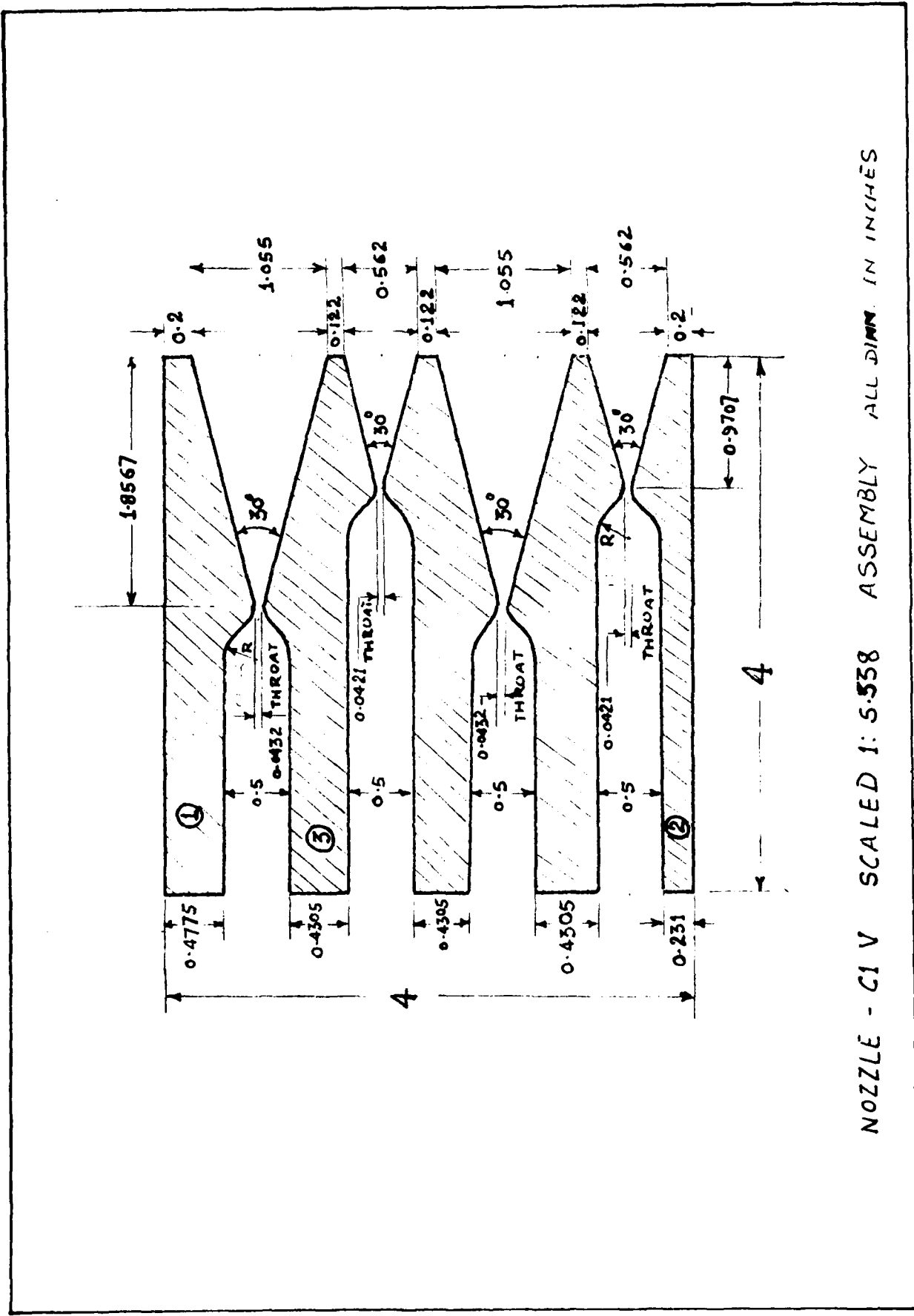


Figure 27. Nozzle No. 3.

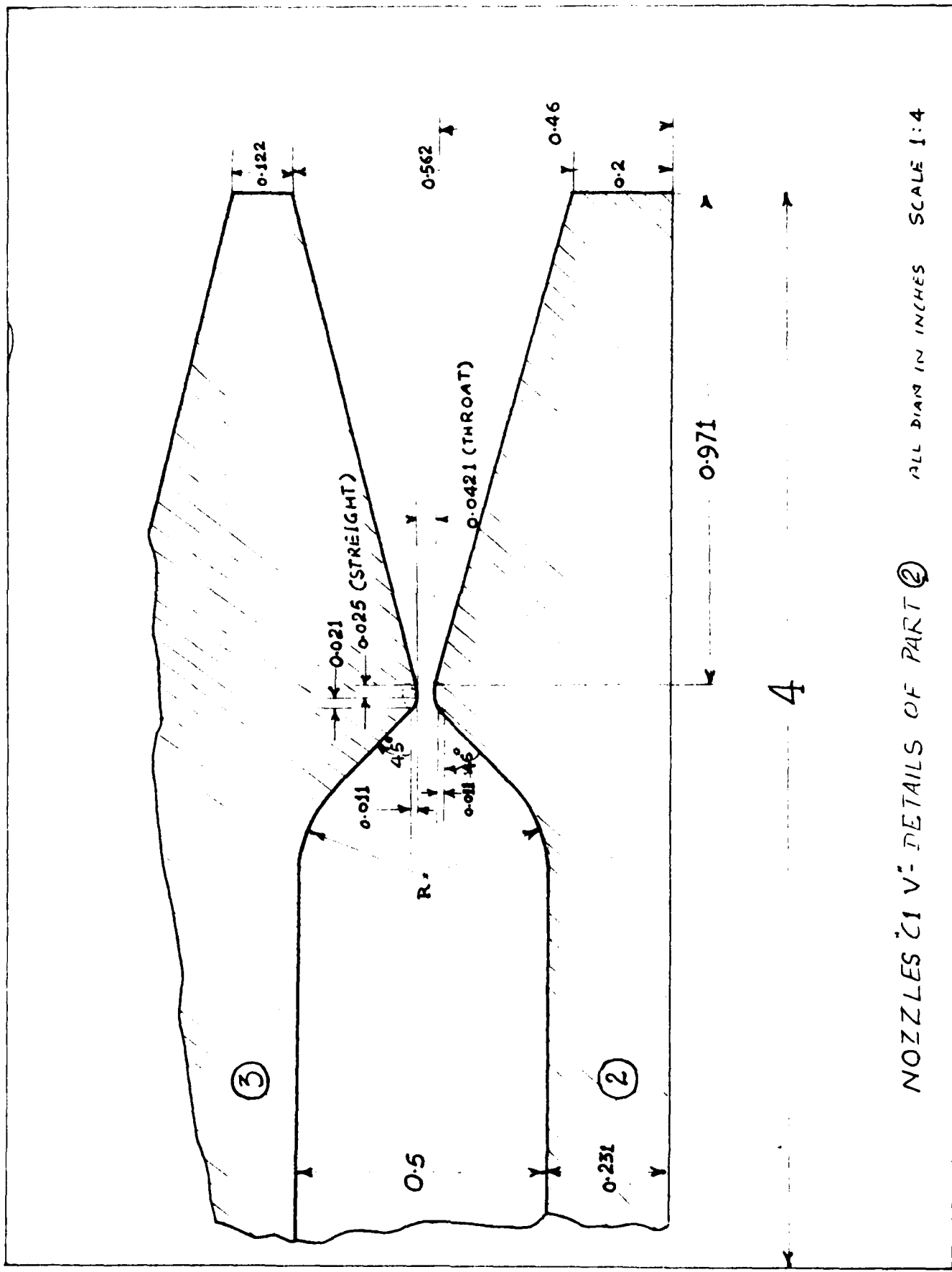


Figure 28. Nozzle No. 3 (Secondary)

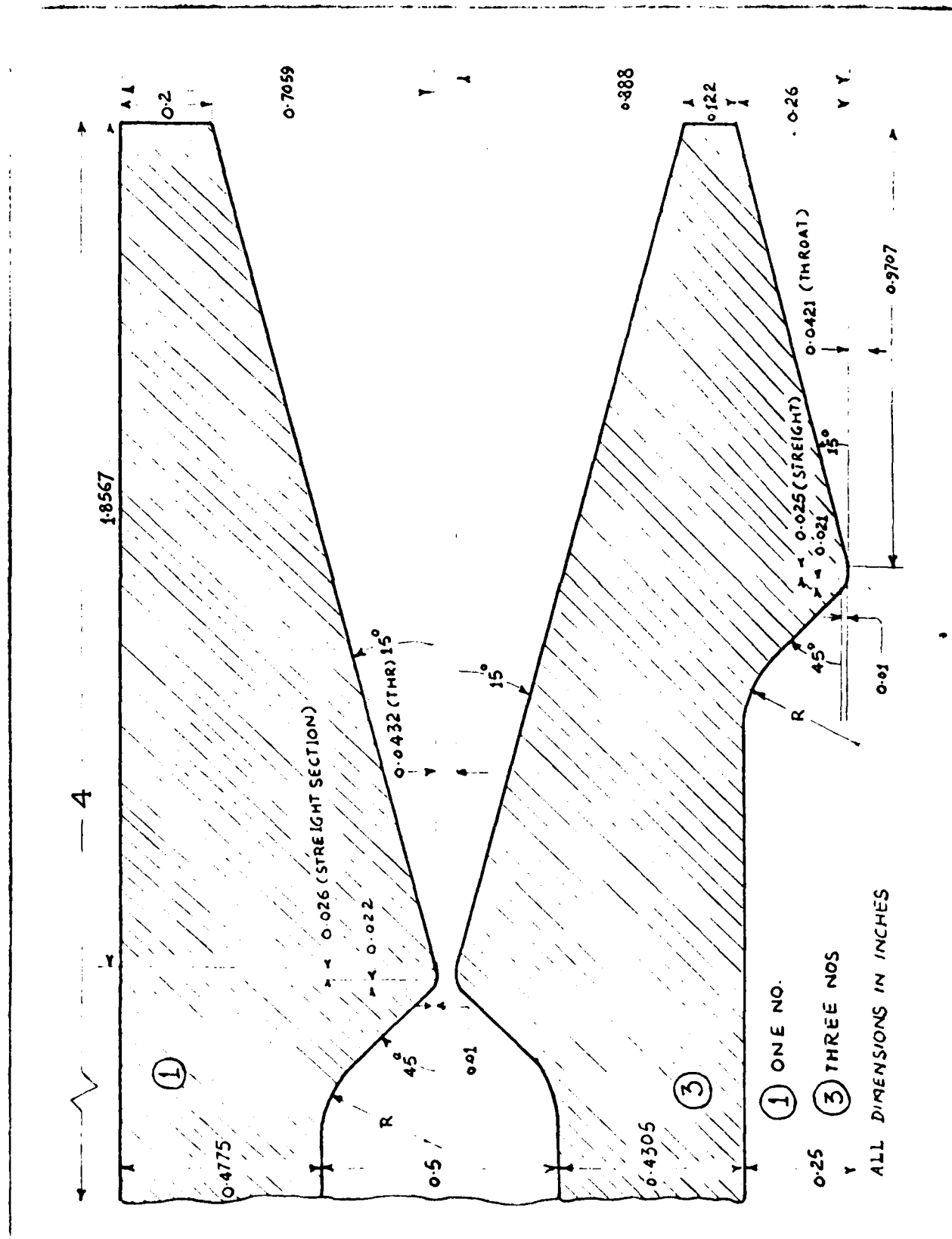


Figure 29. Nozzle No. 3 (Primary).

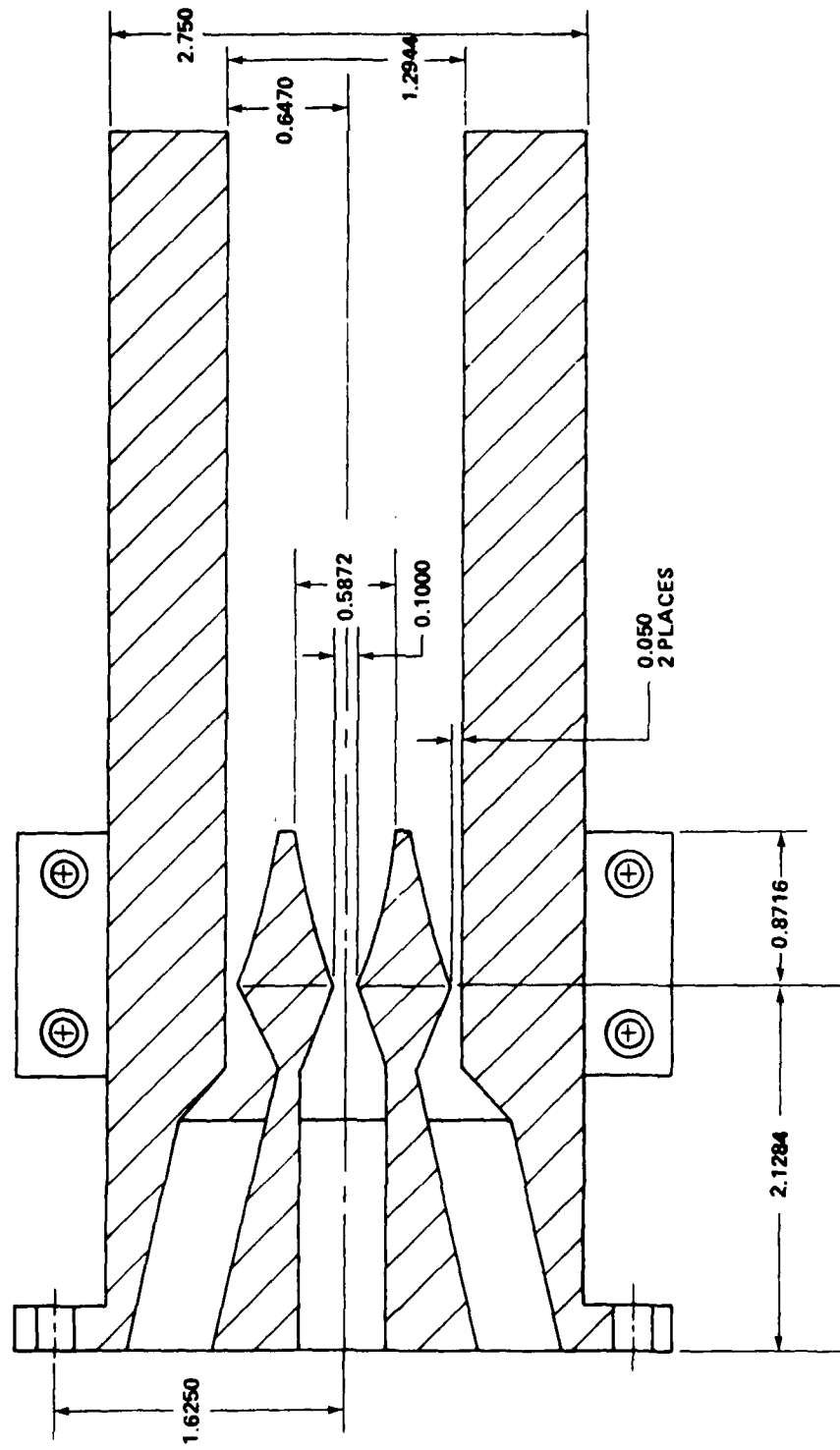


Figure 30. Nozzle No. 4.

TABLE IV. Test Conditions - Nozzle 4 (Secondary)

Secondary Nozzle							
Run No.	psia P_e	C_p/C_v	\bar{M}	ft/sec V_e	P_e/P_c	ft^2/sec $v \times 10^4$	$1/ft$ $R_e/L \times 10^{-6}$
1	.172	1.40	28	2136	0.790	20.57	1.0383
2	.187	1.40	28	2136	1.027	18.95	1.1274
3	.187	1.40	28	2136	0.814	18.95	1.1274
4	.195	1.40	28	2138	0.341	18.23	1.1728
5	.177	1.40	28	2138	0.795	20.05	1.0662
6	.186	1.40	28	2138	0.688	19.03	1.1239
7	.240	1.38	16	2841	0.652	14.54	1.9543
8	-	-	-	-	-	-	-
9	.237	1.38	16	2841	0.963	14.66	1.9376
10	.235	1.38	16	2841	0.951	14.80	1.9194
11	.240	1.38	16	2842	0.971	14.56	1.9519
12	.249	1.38	16	2842	0.452	13.71	2.0598
13	.252	1.38	16	2830	0.652	13.62	2.0778
14	.255	1.38	16	2826	0.659	13.42	2.1059
15	.233	1.38	16	2824	0.804	14.64	1.9295
16	.182	1.40	28	2136	0.361	19.46	1.0977
17	.182	1.40	28	2136	0.268	19.46	1.0977
18	.181	1.40	28	2136	0.314	19.55	1.0927
19	-	-	-	-	-	-	-
20	.078	1.40	28	2138	0.402	45.59	0.4689
21	.078	1.40	28	2138	-	45.59	0.4689
22	.177	1.40	28	2134	0.236	19.93	1.0705
23	.180	1.40	28	2131	0.207	19.49	1.0933
24	.180	1.40	28	2131	0.278	19.49	1.0933
25	.026	-	-	2130	0.048	153.85	0.1591
26	.026	-	-	2134	0.049	154.57	0.1586
27	.025	-	-	2131	0.037	143.06	0.1490
28	.180	1.40	28	2134	0.358	19.59	1.0896
29	.182	1.40	28	2134	0.322	19.59	1.1003
30	.177	1.40	28	2136	0.307	20.00	1.0680
31	.180	1.40	28	2141	0.278	19.77	1.0830
32	.162	1.40	28	2134	0.303	21.74	0.9813
33	.174	1.40	28	2130	0.249	20.20	1.0543
34	.083	1.40	28	2129	0.301	42.34	0.5028
35	-	-	-	-	-	-	-
36	.175	1.40	28	2134	0.307	20.12	1.0606
37	.086	1.40	28	2134	0.315	41.00	0.5204
38	.176	1.40	28	2134	0.303	19.92	1.0692

TABLE V. Test Conditions - Nozzle 4 (Primary)

Primary Nozzle							
Run No.	psia P_e	C_p/C_v	\bar{M}	ft/sec V_e	P_e/P_c	ft^2/sec $v \times 10^4$	$1/ft$ $R_e/L \times 10^{-6}$
1	-	-	-	-	-	-	-
2	-	-	-	-	-	-	-
3	-	-	-	-	-	-	-
4	.279	1.55	11.93	3085	.489	20.03	1.5398
5	.033	1.45	20.92	2387	.147	136.34	0.1751
6	.111	1.42	24.75	2213	.410	38.14	0.5802
7	.084	1.52	14.29	2839	.228	61.64	0.4606
8	.082	1.52	14.39	2830	.680	62.53	0.4525
9	-	-	-	-	-	-	-
10	-	1.40	-	-	-	-	-
11	-	1.40	-	-	-	-	-
12	.247	1.52	14.32	2821	.484	19.03	1.4821
13	.159	1.43	23.25	2264	.412	26.66	0.8492
14	.172	1.40	28.00	2085	.444	23.37	0.8913
15	.074	1.40	28.00	2086	.254	54.75	0.3810
16	.262	1.53	13.62	2903	.522	20.09	1.4449
17	.260	1.61	7.53	3829	.385	27.32	1.4016
18	.178	1.61	7.76	3774	.318	39.20	0.9627
19	.184	1.61	7.66	3798	.561	38.21	0.9940
20	.074	1.40	28.00	2097	.381	55.57	0.3774
21	.074	1.40	28.00	2097	-	55.57	0.3774
22	.147	1.67	4.00	5174	.196	59.09	0.8756
23	.257	1.60	8.08	3097	.295	26.50	1.3949
24	.248	1.40	28.00	2092	.382	16.42	1.2740
25	.156	1.67	4.00	5174	.282	55.61	0.9303
26	.160	1.67	4.00	5174	.299	54.02	0.9577
27	.258	1.61	7.28	3890	.393	28.06	1.3864
28	.180	1.40	28.00	2095	.358	22.67	0.9242
29	.249	1.40	28.00	2095	.441	16.40	1.2771
30	.153	1.67	4.00	5169	.266	56.31	0.9180
31	.275	1.62	7.09	3930	.396	28.49	1.3795
32	.170	1.60	7.92	3730	.318	40.43	0.9227
33	.261	1.61	7.60	3807	.375	26.95	1.4111
34	.073	1.67	4.0	5174	.265	118.92	0.4351
35	.073	1.67	4.0	5175	.392	118.92	0.4351
36	.164	1.67	4.0	5169	.287	52.84	0.9783
37	.073	1.67	4.0	5169	.269	117.90	0.4384
38	.166	1.67	4.0	5169	.286	52.03	0.9936

ANALYSIS

Tests indicated that the contoured nozzles 1, 2 and 4 (Figures 22, 23, 24, 25, 26, and 30) provided better control and repeatability than the straight nozzle 3 (Figure 27 and 28), although the straight nozzle provided occasional high mixing levels. It is expected that the favorable pressure gradient created through the contour and the stabilized boundary layer on the internal walls of the contoured nozzles provided the consistent flow conditions downstream. The less stable boundary layer internal to the straight nozzle increased the chance of separation, adverse compression shocks and thus variable and unpredictable flow conditions downstream. The alternate large and small nozzle arrangement was not found to greatly influence mixing. Data and pictures suggested that the comparison of flow field mixing downstream of nozzles 1, 2 and 4 were not particularly sensitive to geometry.

The study concerning density mapping was only partially successful in that the procedure was identified and applied to general flow fields; however, applications to conditions of this study was hampered by the loss of the Argon laser at a critical point in the study. Quantitative data was therefore not obtained as to the evaluation and diagnosis of flow field mixing.

Qualitatively, test nozzle 4 provided much information on mixing. For example, the high mass flow of N_2 and He mixture in the center nozzle (Figure 31), which provided a lower molecular weight and higher Mach number there, reduced the mixing significantly in the near field. Density level variations of the same flow conditions (observed in the Figure 32 interferogram) also indicates low level mixing. The sensitivity of flow conditions is observed in Figure 33, where good mixing is occurring. The only significant difference

in the flow conditions from Figures 31 and 32 was the exit pressure conditions for the center nozzle (which was lowered) that forced rapid inward flow from the outer nozzles. Figure 34 is an indication of moderate to poor mixing. Here the mass flow of adjacent nozzles were nearly the same.

As a base, Figure 35 was run with near zero flow rate through the center nozzle and methane CH_4 on either side at 21 grams/sec, which should have maximized the divergence of the outer nozzles in the near field, yet little of this occurred. A similar flow pattern occurred for matching all flow properties for the nozzles (Figure 36). Figures 37 and 38 are horizontal and vertical (knife edge) schlierens of high center mass flow rates, low exit pressures of the center nozzle and a relatively high cavity pressure, providing moderate to good mixing. Lowering the cavity pressure, matching the flow rates, but increasing the exit pressure differences provided very good diffusion mixing (Figure 39), which also reduced the shock strength and viscous effects.

As a check on the effect of maximizing the flow rate of the exterior nozzles, Figure 40 provides additional evidence that this condition does not enhance mixing. Conversely, increasing the flow rate of the center significantly, plus a higher cavity pressure (about 3 times) provided excellent mixing of the flow streams from the nozzles (Figure 40).

Demonstrated in the tests was the mean bulk flow direction change toward the nozzle that provided the least momentum flux and was typical for all the runs and dominant in the non-equilibrium zone of the near field, which occurred up to 10 diameters downstream. Solutions for the non-equilibrium zone, assuming a laminar mixing layer was obtained from the momentum integral method and provided approximations and insight to the mixing zone, layer thickness and length,

with reasonable agreement with tests. Approximations were also obtained for the turbulent mixing layer length, suggesting the test conditions were mostly transitional to turbulent in the non-equilibrium zone.

BIBLIOGRAPHY AND REFERENCES

1. J.C. Polanyi, "Proposal for an Infrared Laser Dependent on Vibrational Excitation," J. Chem. Phys. 34 (1), 347-347 (1961).
2. J.V.V. Kasper and G.C. Pimentel, "HCL Chemical laser," Phys. Rev. letters 14 (10), 352-354 (1965).
3. W.R. Warren, Jr., "Reacting Flow and Pressure Recovery Processes in HF/DF Chemical Lasers," U.S. Air Force Report No., SAMS0-7R-74-68.
4. J.D. Trolinger, "Laser Instrumentation for Flow Field Diagnostics," AGARD-AG-186, March, 1974.
5. F.C. Jehoda and R.E. Sieman, "Holographic Interferometry," Los Alamos Scientific Laboratory Report LA-5058-MS, April, 1972.
6. G. W. Stokes, An Introduction to Coherent Optics and Holography, Academic Press, New York, 1966.
7. H.J. Caulfield and Sun Lu, The Applications of Holography, John Wiley and Sons, 1970.
8. C. R. Wimberly, L. B. Thorn and G. W. Butler, "Chemical Laser Flow Simulation and Mixing Studies Using Holographic Flow Visualization Techniques", U. S. Army Missile Command Technical Report RK-73-14, August, 1973.
9. C. R. Wimberly and R. H. Lin, "An Investigation of the Turbulent Mixing Phenomena in the High Speed Exhaust Flow Field of the Chemical Laser", Final Research Report ARO Grant No. DAH C04 74G 0046, December, 1974.
10. J. D. Trolinger and J. E. O'hare, "Aerodynamic Holography", AEDC-TR-70-44, August, 1970.
11. Collier, Burkhardt, and Lin, Optical Holography, Academic Press, New York, 1971, pp. 170-174.
12. J. P. Holman, Experimental Methods for Engineers, McGraw-Hill Book Company, New York, 1966.
13. D. J. Spencer and R. L. Varwig, "Experimental CW Chemical Laser Studies", AIAA Journal Vol. 11, No. 7, July, 1973.

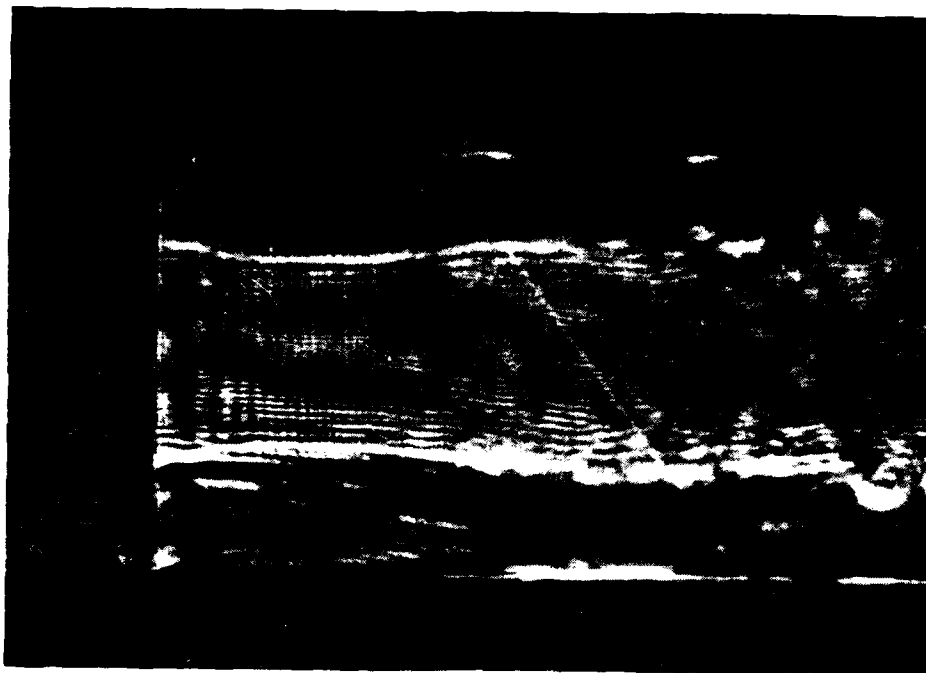


Figure 31. Shadowgraph of Mach 3 Test (Run 1).

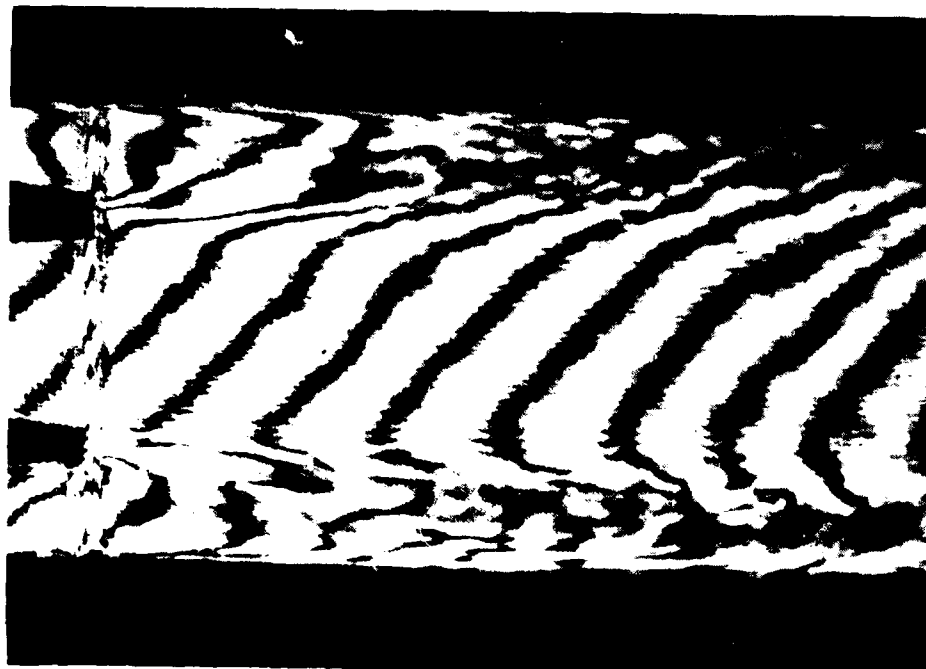


Figure 32. Interferogram of Test Flow (Run 3).

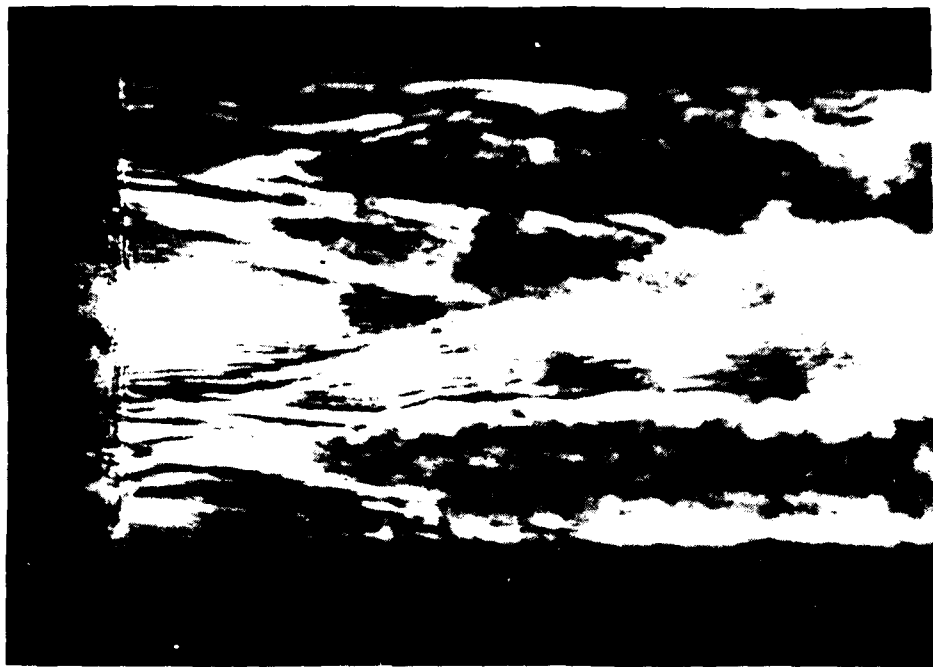


Figure 33. Schlieren of Test Flow (Unmatched Flow - Run 5)

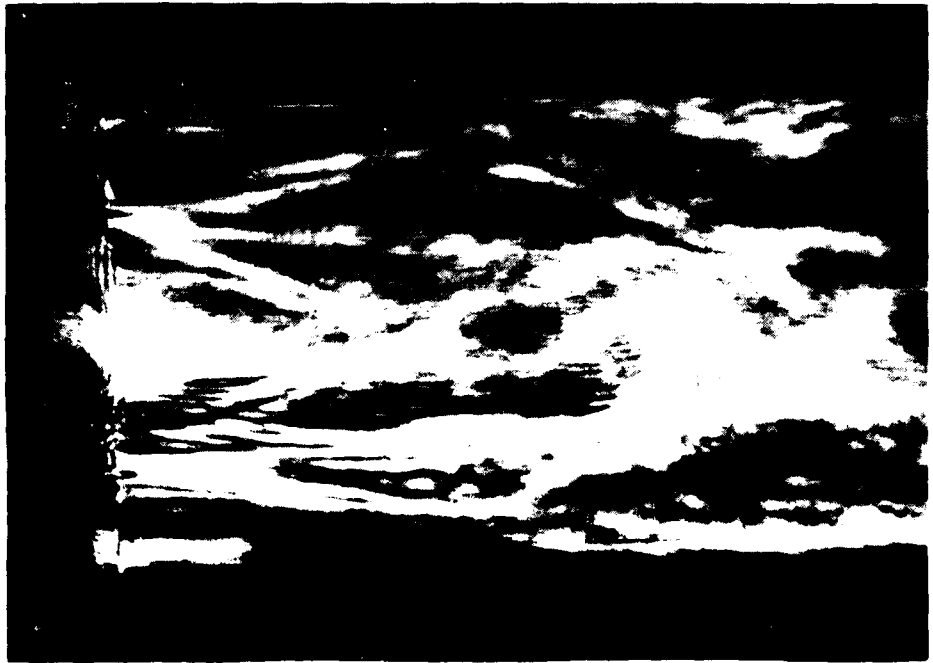


Figure 34. Schlieren of Test Flow (Matched Flow - Run 6).

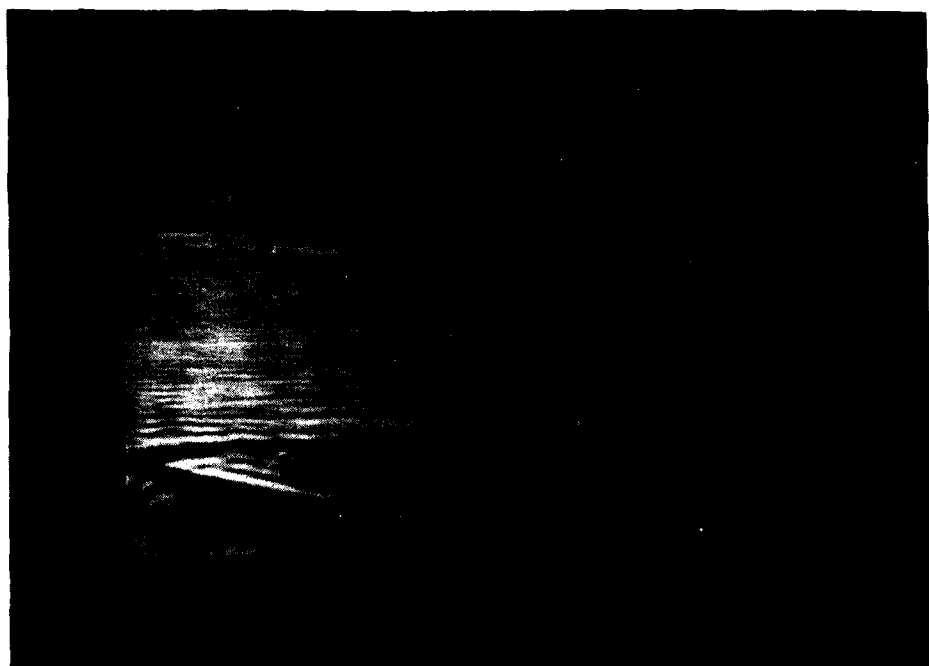


Figure 35. Shadowgraph of Test Flow (Zero Center Flow - Run 9).



Figure 36. Shadowgraph of Test Flow (Matched Flow - Run 11).



Figure 37. Schlieren of Test Flow (Horizontal Knife Edge - Run 12).



Figure 38. Schlieren of Test Flow (Vertical Knife Edge - Run 14).



Figure 39. Shadowgraph of Test Flow (Run 15).



Figure 40. Schlieren of Test Flow (Run 17).

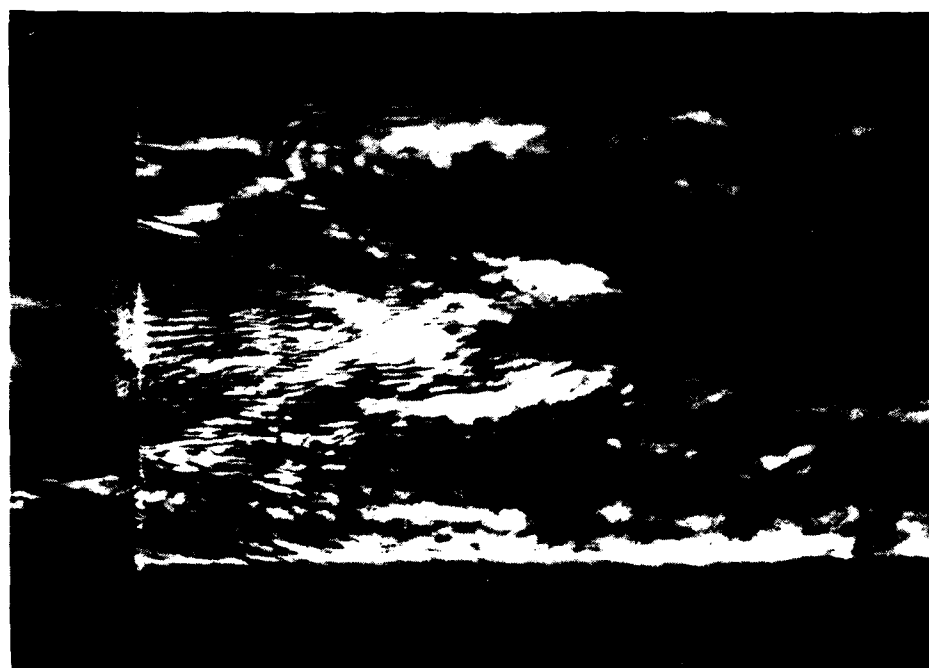


Figure 41. Schlieren of Test Flow (Run 20).

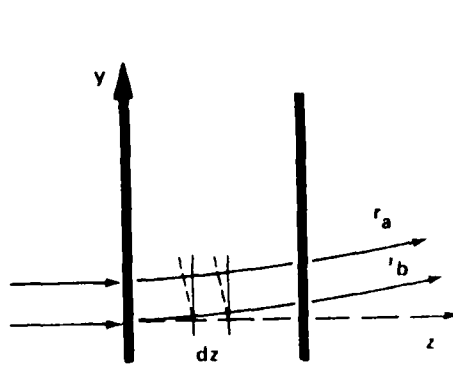
Appendix A

Shadow, Schlieren and Holographic Fundamentals

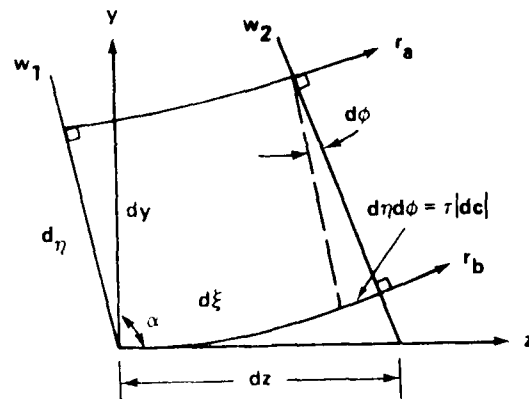
The character of gas dynamics makes it possible to view turbulence, shock patterns, boundary layers and other phenomena in the flow, caused by variations in properties, particularly density, in several ways. This is possible because of the manner in which light passes through the medium being investigated. The figures below illustrate how light may be refracted through a gaseous medium, where the density, ρ , increases in the positive y direction.

The index of refraction $n = c_0/c = 1 + \rho \theta/\rho_s$.

The angle of refraction $c = \int_0^L d\phi$



TEST SECTION



ELEMENT

From geometry, $dn = dy \sin \alpha$, and $dz = dz \sin \alpha$. And since $c = c_0/n$, we can write $\frac{(dc)}{dy} = \frac{c}{n} \frac{dn}{dy}$

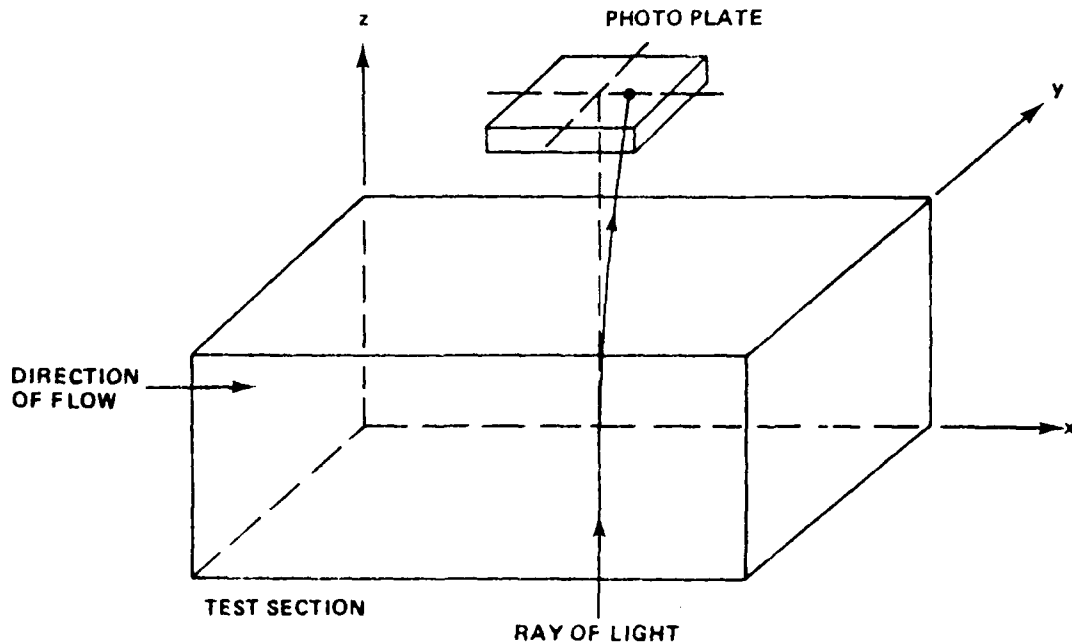
where $d\xi = \tau c$, the distance traveled along r_b .

The angle of refraction can thus be written:

$$\begin{aligned}
 \phi &= \int dt = \int \frac{dc}{ds} = \int \frac{\tau |dc|}{dy \sin \alpha} \\
 &= \int \frac{1}{\sin \alpha} \left(\frac{c}{n} \frac{dn}{dy} \right) = \int \frac{ds}{\sin \alpha} \frac{1}{n} \frac{dn}{dy} \\
 &= \int_0^L \frac{1}{n} \frac{dn}{dy} dz = \int_0^L \frac{ds}{n_s} \frac{1}{n} \frac{dn}{dy} dz
 \end{aligned}$$

From a three dimensional view point, as shown in figures below, the direction of refracted light will depend on the direction of flow. For the case below the flow is the x direction, while the light beam is in the z direction. The resulting angles of refraction in the y and x directions can thus be written.

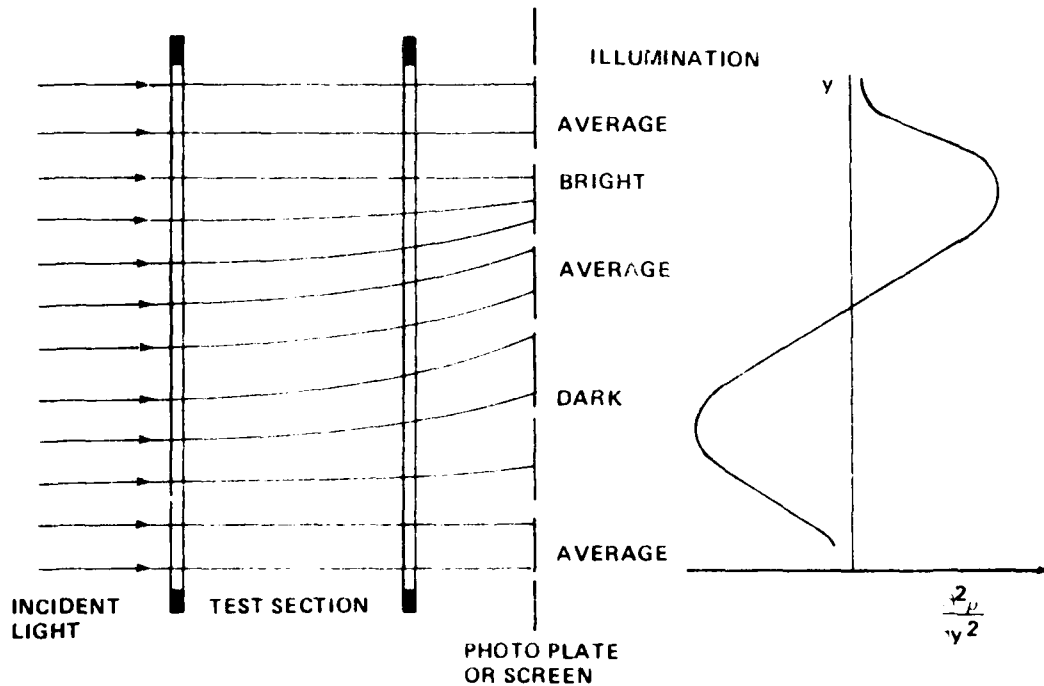
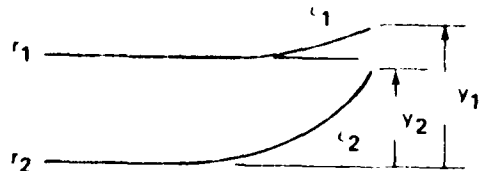
$$\phi_x = \frac{1}{n} \int_0^L \frac{dn}{dx} dz = \frac{\beta}{n_s s} \int_0^L \frac{dn}{dx} dz \quad \phi_y = \frac{1}{n} \int_0^L \frac{dn}{dy} dz = \frac{\beta}{n_s s} \int_0^L \frac{dn}{dy} dz$$



The shadow method for making shadowgraphs is illustrated below.

Here, the light is refracted as it passes through the test section, providing light and dark regions on the photo plate or screen. The shadow effect (dark and bright regions) depend on the relationship.

$$\lim_{\Delta y \rightarrow 0} \frac{\Delta \epsilon}{\Delta y} \frac{y_2 - y_1}{y_2 - y_1} = \frac{\partial \epsilon}{\partial y}$$



$$\text{At the test section } \frac{d\epsilon}{dy} = \frac{L_B d\epsilon}{\rho s dy}$$

$$\text{The illumination } I = \frac{\partial \epsilon}{\partial y}$$

We may therefore write in plane flow

$$I = \frac{1}{s} \frac{\partial^2}{y^2} + \frac{1}{s} \left[\frac{2}{y^2} + \frac{2}{z^2} \right]$$

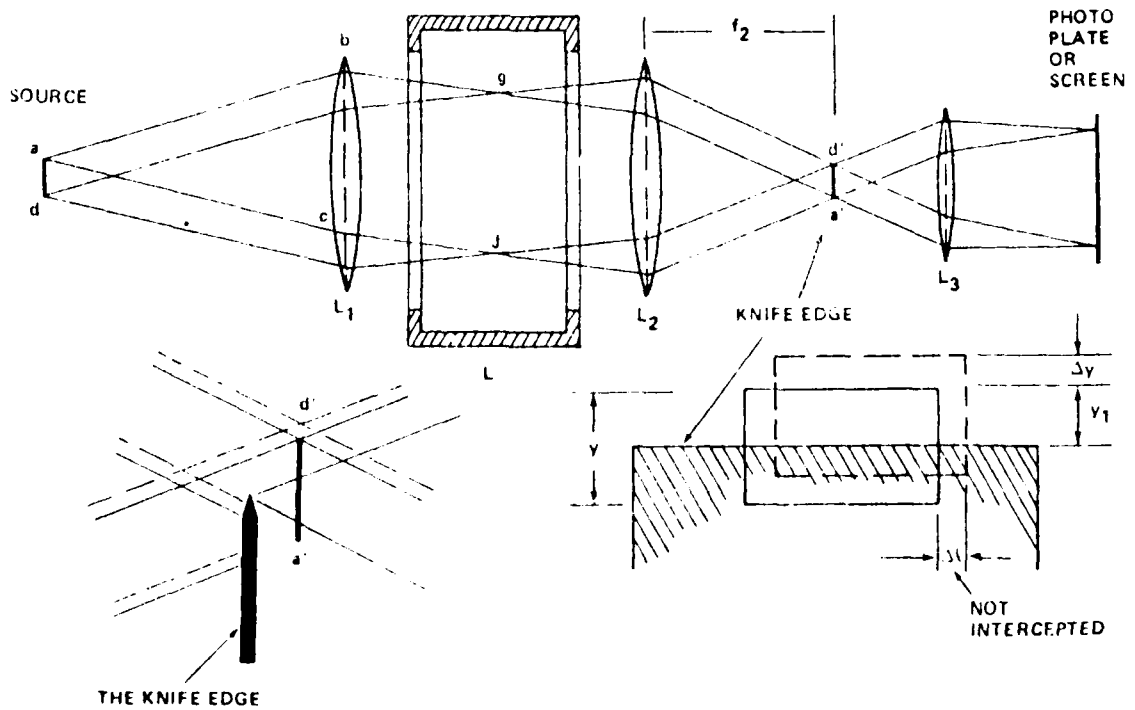
Schlieren photographs are characterized by symmetric light and dark regions caused by density gradients in the direction of the light. The figure below illustrates a Schlieren system for pencils of light as they proceed through a test section of uniform density. A knife edge placed at the focal point intercepts the light. At the knife edge, a portion of the light is refracted by a distance $\Delta y = f_2 \epsilon$. The contrast illuminated on the photo plate is

$$C = \Delta I / I$$

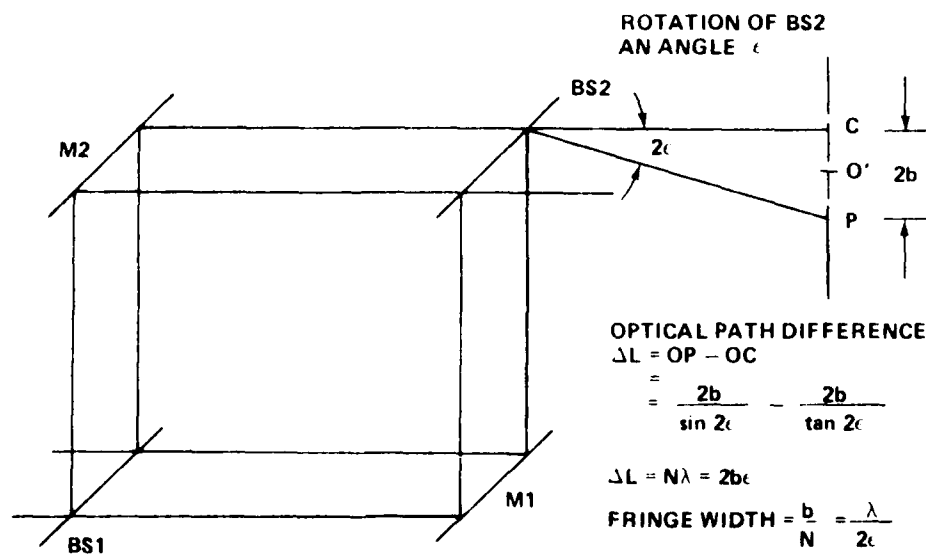
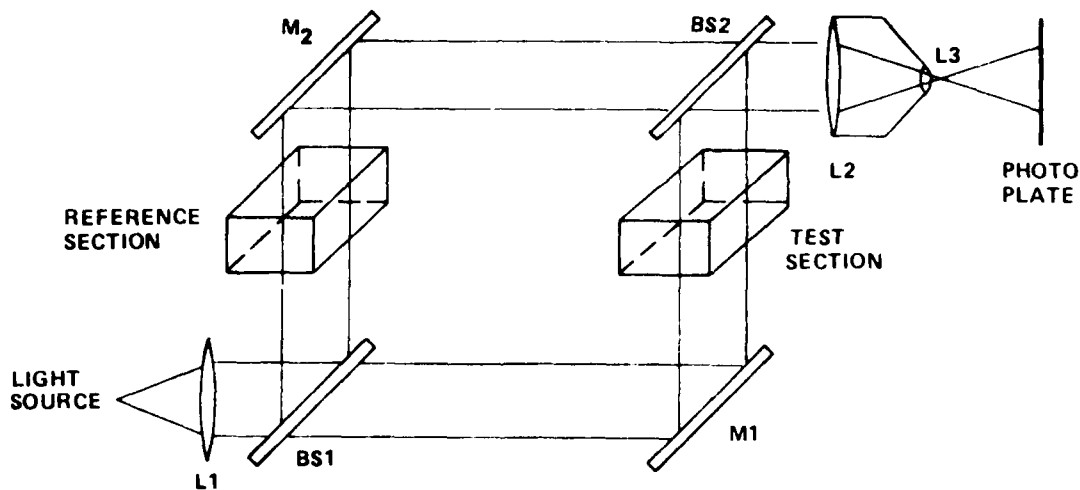
where, $C = \Delta y / y_1 = f_2 \epsilon / y_1$, and $\epsilon = \frac{l}{n_1} \frac{\partial n}{\partial y}$

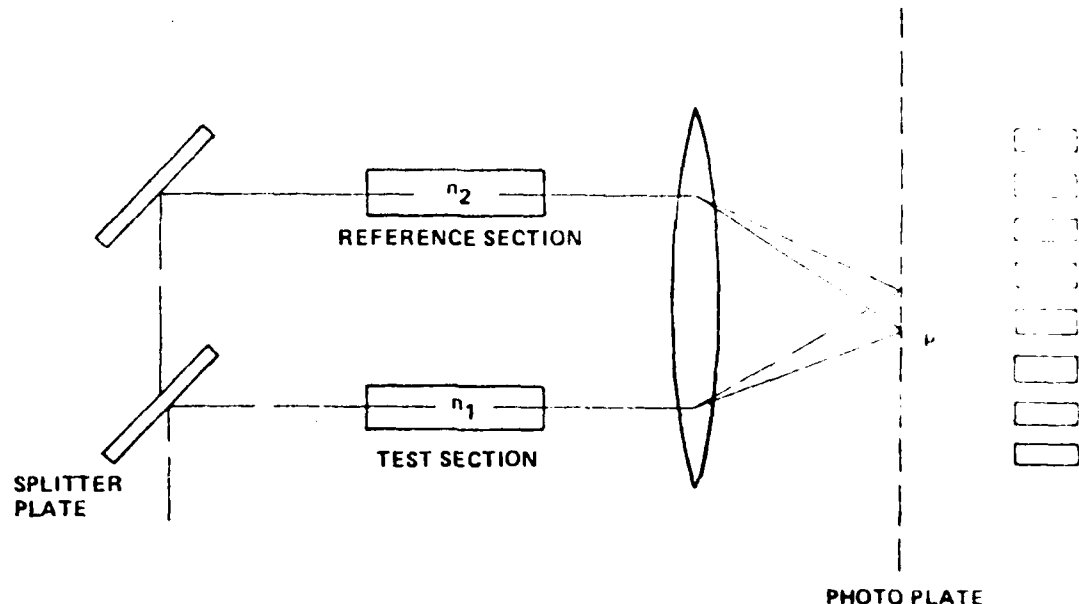
we can thus write a relationship depicting the contrast

$$C = \frac{f_2 l^2}{n_1 y_1 f_1} \frac{\Delta \epsilon}{\Delta y}$$



The fundamental operations of the interference method, are illustrated in the figures below. As shown, light travels to a beam splitter (BS1), generally passing 50% of the light. The separated light then travels to respective mirrors, each traveling through different media. The light is then gathered at the second beam splitter (BS2), each light ray possessing a different character because of their now different optical paths. The light finally passes through a lens and onto a photo plate that illuminates the fringe patterns caused by the different wave character. The fringe and density relation for the interference method is shown below.



Fringe and Density Relation

If $n_1 > n_2$, then $c_2 > c_1$

$$n_1 = \frac{c_0}{c_1} = 1 + \frac{\beta_1}{s}$$

The additional time to traverse the test section is

$$n_2 = \frac{c_0}{c_2} = 1 + \frac{\beta_2}{s}$$

$$\Delta t = \frac{L}{c_1} - \frac{L}{c_2} = \frac{L}{c_0} (n_1 - n_2).$$

Change in optical path is $\Delta L = c_0 \Delta t = L(n_1 - n_2) = N\lambda$

$$N = \frac{L}{\lambda} (n_1 - n_2)$$

$$N = \frac{\beta L}{\lambda} \left(\frac{n_1 - n_2}{s} \right) = \text{number of fringes.}$$

If density varies along a ray

$$N = \frac{\beta}{\beta_s} \int_0^L (n_1 - n_2) ds$$

Appendix B

Density-Refractive Index Relationship

Density-Refractive Index Relationship

There are three empirical expressions that have been proposed for the relationship between the refractive index n , for a particular wavelength of radiation, and the density, ρ , of a given transparent body. These expressions, in historical order are:

$$\text{Newton-Laplace} \quad (n^2 - 1)/\rho = \text{Constant}$$

$$\text{Gladstone-Dale} \quad (n - 1)/\rho = \text{Constant}$$

$$\text{Lorenz-Lorentz} \quad (n^2 - 1)/(n^2 + 2)\rho = \text{Constant}$$

The first expression was developed by Newton and gave a reasonable value for most liquids when the temperature was varied, and was partially based on the emission theory of light. Laplace inferred the same expression from theoretical considerations based on the form of the undulatory theory accepted at his time. As a result of experimentation on water and its vapor, it was considered that the relationship did not hold when a change of state occurred.

Better agreement with experimental facts was obtained with the second experimental expression, which was proposed by Gladstone and Dale (1858, 1863) as a result of experiments with water and carbon disulphide at different temperatures. Sutterland (1889) attempted to give a theoretical basis for this relation, but without much success.

The third relation was independently derived by Lorenz (1880) of Copenhagen and Lorentz of Amsterdam, from entirely different theoretical approaches. Lorenz considered the passage of light through media consisting of spherical molecules immersed in an ether having the properties of an elastic solid. Lorentz derived the same expression from his own theory of electrons considered in relation to Maxwell's system of equations for electromagnetic theory of light. Lorenz and others have found it particularly successful in correlating the facts when a liquid passes to the gaseous state.

The experimental comparison of the three relations in the case of gases is not so easily made as in the case of liquids, although a considerable amount of research has been devoted to the subject because of the ease with which the density of a gas may be varied by alterations of temperature and pressure. The refractivity of gases at normal densities is relatively small. The first and third relations then reduce, as a first approximation to the Gladstone-Dale equation.

Interferogram Reduction

The final result of any of the six techniques of holographic interferometry is an interferogram with interference fringes.⁴

The next step is to obtain the density distribution by a suitable reduction from the interferogram. Before we can do this, we have to establish the fringe-shift density relationship.

The following are a few basic assumptions made from geometrical and physical optics:

- 1) In a homogenous, isotropic medium a beam of light may be analyzed into rays which are represented either as vectors or straight lines in 3 space.
- 2) A monochromatic ray of light consists of a sinusoidal disturbance of frequency v and wavelength λ propagating along the normal to the direction of vibration with velocity u .
- 3) $\lambda v = u$ is satisfied where v is constant and λ, u are functions of the coordinates.
- 4) Index of refraction 'n' is related to velocity by $n = c/u$ where c is velocity of light in vacuum.
- 5) For gaseous media at moderate pressures there is a direct relation

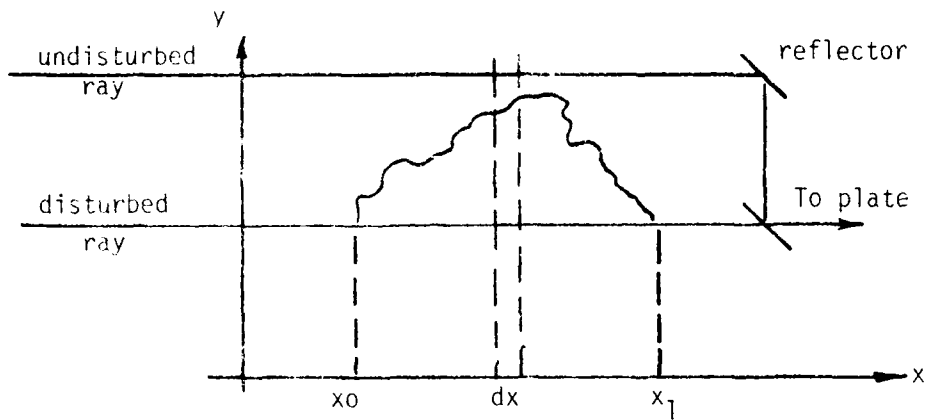
between density increments $\rho - \rho_0$ and index of refraction $n - n_0$, thus,

$$n - n_0 = k(\rho - \rho_0) \quad (1)$$

where k is the Gladstone-Dale constant.

6) For axisymmetric flows, the refraction of any ray in the disturbed beam is negligible.

With these preliminaries, we can now derive the fringe shift equation.



Consider a general density disturbance in one beam of a Mach-Zehnder interferometer. Coordinate directions are defined by an orthogonal right-hand triad with x parallel to the interferometer beam and y vertical as in the Figure above.

If the index of refraction function $n(x, y, z)$ has only a finite number of discontinuities, the fringe shift $\delta(y, z)$ is given by

$$\delta(y, z) = \frac{1}{\lambda} \int_{x_0}^{x_1} (n - n_0) dx = \frac{k}{\lambda} \int_{x_0}^{x_1} (\rho - \rho_0) dx \quad (2)$$

Where n_0 and ρ_0 are the reference index of refraction and density in the undisturbed beam and λ is the vacuum wavelength of light.

To prove (2), we observe that the optical pathlength of the disturbed ray

in λ wavelengths is

$$N_d = \int_{x_0}^{x_1} \frac{dx}{\lambda} = \int_{x_0}^{x_1} \frac{n dx}{\lambda} \quad \text{where } \lambda \text{ is the vacuum wavelength of light.}$$

The difference $N_d - N_0$ gives the number of multiples of 2π by which the two rays differ in phase when recombined. This number is equal to the fringe shift $\delta(y, z)$.

$$\text{i.e. } N_0 = \int_{x_0}^{x_1} \frac{dx}{\lambda_0} = \int_{x_0}^{x_1} \frac{n_0 dx}{\lambda^*}$$

Two-Dimensional Density Fields

If $n = n(y, z)$ and $(\rho - \rho_0) = \frac{n - n_0}{k}$, then for two dimensional flues,

$$\delta(y, z) = \left[\int_{x_0}^{x_1} (\rho - \rho_0) dx \right] \frac{2\pi k}{\lambda^*} \quad (3)$$

$$= \frac{2\pi k}{\lambda^*} (\rho - \rho_0) [x]_{x_0}^{x_1} \quad (4)$$

the flue is in the y-z plane, the term $(\rho - \rho_0)$ can be taken out of the integral sign. This means that, the density distribution is two-dimensional in the y-z plane.

$$\delta(y, z) = \frac{2\pi k}{\lambda^*} \int_{u_\lambda}^{u_n} (\rho - \rho_0) (x_1 - x_0) \quad (5)$$

$$\text{or } (\rho - \rho_0) = \frac{\delta(y, z) \lambda^*}{2\pi k (x_1 - x_0)} \quad (6)$$

$$\text{or } \rho(y, z) = \rho_0 + \frac{\delta(y, z) \lambda^*}{2\pi k (x_1 - x_0)}$$

Thus knowing $\delta(y, z)$ from the interferogram and knowing ρ_0 we can determine $\rho(y, z)$.

Determination of Fringe-Shifts from Interferograms

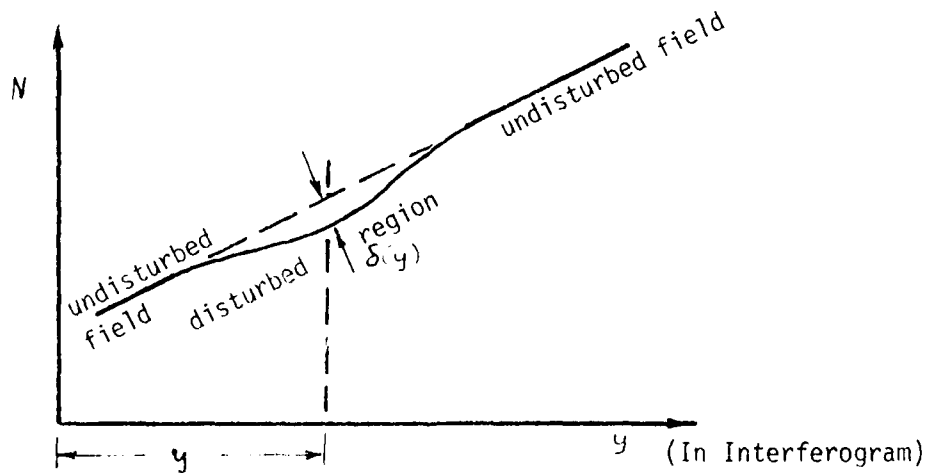
To obtain the graphical plot of the fringe number functions, the negative is used in a photo enlarger to image directly upon graph paper. With the negative adjusted to match the scale of the paper, the positions of the maximum and minimum of the figures along the desired cross-section are determined

visually. Initial fringe numbering is arbitrary. Commencing with a fringe well to one side of the field and proceeding across the field, the length requires representing integer values of the fringe number.

If the fringe number N is plotted against position y , a straight line is obtained for fringes in the undisturbed field. With flow in the test section established, the plot deviates from a straight line in the disturbed part of the field, so that at each y value the fringe shift is given directly by the difference in the ordinates of the two curves. The fringe shifts are actually not plotted out but calculated from the equivalent equation;

$$\delta(y) = N_I \left[y \left(\frac{N_d - N_0}{y_1 y_0} \right) + N_0 - y_0 \left(\frac{N_1 - N_0}{y_1 y_0} \right) \right] \quad (7)$$

This equation is obtained as follows:



The fringe shift $\delta(y)$ at any point a distance y from the origin is given by

$$\delta(y) = N' - N$$

where N' -- fringe number in the disturbed region

N -- fringe number in the undisturbed flow

Now, we know that in the undisturbed region the fringes are parallel and equally spaced. Hence, we can assume N to be linearly related to y , that is

$$N = Ay + B \quad (8)$$

$$N = N_0 @ y = y_0$$

$$N = N_1 @ y = y_1$$

Where N_1 and N_0 are two fringes close together in the undisturbed region, close to the boundary of disturbance

y and y_0 are the correct positions of N_1 and N_0 in the particular cross-section being considered.

$$\begin{aligned} N_0 &= Ay_0 + B & A &= \frac{N_1 - N_0}{y_1 - y_0} ; & B &= N_0 y_0 \left(\frac{N_1 - N_0}{y_1 - y_0} \right) \\ N_1 &= Ay_1 + B & & & & \end{aligned}$$

$$\delta(y) = N(Ay + B) \quad (9)$$

The sign is to be chosen so that positive fringe shifts result from retarded rays, where the average density through the flow is greater than in the undisturbed region. The form of (9) may be varied to suit the computing machine.

After calculation of $\delta(y)$ for different values of y from (9), a smooth curve can be drawn through the points $[y, \delta(y)]$.

Appendix C

Computer Programs
Including Subroutines

```

5      REAL MU(161),MUPOS,MA,MB,MU120,MU220,MUS,ME(161)
6      DIMENSION U(161,162),ZUO(161),A(162),U1(161),U2(161),VES(161)
7      ,PD(161),P(161),DISP(161),AI(161),TY(161),TY1(161),T(161)

8      READ (2,15,END=9999) (AI(JI),JI=1,161,4)
9      READ (2,11,END=9999) MA,MB,CPA,CPB,CVA,CVB,AM,BM,TO,PO,
10     MU220,MU120,D2,D1
11     FORMAT (6F10.4)
12     FORMAT (6E20.5)
13     FORMAT (1X,161F10.0)
14     FORMAT (10F5.4)

15     CALL HEATR (MA,MB,CPA,CPB,CVA,CVB,AM,BM,R,CM,CP)
16     CALL THROAT (R,CM,TO,PO,TS,PS,ZUOS,US)
17     CALL VISCOS (TS,MB,MA,MU120,MU220,D1,D2,BM,AM,MUS)

18     VEL0=US*.3048
19     TK=(TS-460-32)*5./9+273
20     ZUOG=ZUOS*453.59/(30.48)**3.
21     MUPOS=MUS*14.882
22     PTOR=PS*760/14.7
23     WRITE (3,12) MA,MB,CM,R,TO,CP,VEL0,TK,ZUOG,MUPOS,PTOR

24     DX=.8716/(160.*.1)
25     D=.1/12.
26     RS=.1/2./12.
27     TSI=0.5
28     DSI=TSI/160.
29     PD(1)=PS*144*32.2/(ZUOS*US**2.)
30     RES=ZUOS*US*D/MUS
31     DO 1 JI=2,162
32     U(1,JI)=1.
33     DO 2 II=1,161
34     U(II,1)=0.
35     DISP(1)=0.
36     DO 16 JI1=3,159,4
37     AI(JI1)=(AI(JI1-2)+AI(JI1+2))/2.
38     DO 17 JI2=2,160,2
39     AI(JI2)=(AI(JI2-1)+AI(JI2+1))/2.

40     DO 9 II=1,10
41     NW=1
42     CALL PRESS(PS,R,PO,AI,DISP,P)
43     DO 6 JI1=1,171
44     ZUO(JI1)=1.
45     MU(JI1)=MUS
46     T(JI1)=TS

```

C THIS SUBPROGRAMME IS USED TO PREDICT PROPERTIES
C AT THROAT FROM SOME RESERVOIR CONDITIONS

SUBROUTINE THROAT (GAMA, CM, TO, PO, TS, PS, ZUOS, US)

```
TO=TO*9/5+32+460
ZU00=PO*144*(CM/1544)/TO
TS=2./(GAMA+1.)*TO
PS=(2./(GAMA+1.))**((GAMA/(GAMA-1.))*PO
ZUOS=(PS/PO)**(1/GAMA)*ZU00
US=SQRT(GAMA*1544/CM*32.2*TS)
RETURN
END
```

C THIS SUBPROGRAMME IS USED TO DETERMINE
C SPECIFIC HEAT RATIO AND MOLECULAR WEIGHT OF MIXED GASES

SUBROUTINE HEATR (MA, MB, CPA, CPB, CVA, CVB, AM, BM, R, CM, CP)

```
REAL MA, MB
CP=(MA*CPA+MB*CPB)/(MA+MB)
CV=(MA*CVA+MB*CVB)/(MA+MB)
R=CP/CV
CM=(MA+MB)/(MA/AM+MB/BM)
RETURN
END
```

C THIS SUBPROGRAMME IS USED TO DETERMINE VISCOSITY OF
C MIXED GASES AT TEMPERATURE T

SUBROUTINE VISCOS (T, M2, M1, MU120, MU220, D1, D2, W2, W1, MU)

```
REAL M1, M2, MU1, MU2, MU120, MU220, MU
T20C=528.
DELMU1=(T-T20C)*D1*5/9.
DELMU2=(T-T20C)*D2*5/9.
MU1=MU120+DELMU1
MU2=MU220+DELMU2
X1=(M1/W1)/(M1/W1+M2/W2)
X2=(M2/W2)/(M1/W1+M2/W2)
IF (X2.EQ.0.) GO TO 1
PH12=(1+(MU1/MU2)**0.5*(W2/W1)**0.25)**2.
PH12=PH12/(8.**0.5)/(1+W1/W2)**0.5
PH21=(1+(MU2/MU1)**0.5*(W1/W2)**0.25)**2.
PH21=PH21/(8.**0.5)/(1+W2/W1)**0.5
MU=MU1/(1+X2*PH12/X1)+MU2/(1+X1*PH21/X2)
GO TO 2
1 MU=MU1
2 MU=MU*6.7197E-08
RETURN
END
```

```

DO 5 I=1,160
PR=P(I+1)
PD(I+1)=P(I+1)*144.*32.2/(ZU0S*US**2.)
DO 3 J2=1,161
3   A(J2)=ZU0(J2)*U(I,J2)*MU(J2)/MUS
DO 4 J=2,161
TERP=(-1./(ZU0(J)*U(I,J)))*(PD(I+1)-PD(I))/DX
AA1=(A(J)+A(J+1))/2.
AA2=(A(J)+A(J-1))/2.
TERMU=AA1*(U(I,J+1)-U(I,J))-AA2*(U(I,J)-U(I,J-1))
TERMU=TERMU/(DSI**2.*RES)
4   U(I+1,J)=U(I,J)+DX*(TERP+TERMU)
U(I+1,162)=U(I+1,160)
DO 8 J3=1,161
U1(J3)=U(I+1,J3)
T(J3)=T0-(U1(J3)*US)**2./(2.*32.2*778.*CP)
ZU0(J3)=P(I+1)*144./((1544./CM)*T(J3))/ZU0S
MU(J3)=MUS*(T(J3)/TS)**/75
VES(J3)=SQRT(R*1544/CM*32.2*T(J3))/US
8   CONTINUE
CALL DISPLE (D,ZU0,DSI,U1,VES,TY,TTY,TY1,ME,DISP2)
IF (I/EQ.160) GO TO 50
DISP(I+1)=DISP2
50  CONTINUE
IF (II.LT.3) GO TO 5
IF (I.NE.NW) GO TO 5
NW=NW+40
DX1=DX*.1/12.
DX2=DX1*30.48
RS1=RS*30.48
X1=DX1*I
X2=X1*30.48
XDR=X1/RS
PTOR=P(I+1)*(760/14.7)
DPDX=(P(I+1)-P(I))/(DX*.1/12)*(760/14.7)/30.48
WRITE (3,14) II,X1,X2,RS1,TTY
WRITE (3,20) I,XDR,PTOR,DPDX,DX1,DX2
DO 30 K=1,20
YDR=AI(I+1)/.05-TY(K)/(RS*12.)
VELO=U1(K)*US*.3048
TK=(T(K)-460-32)*5./9+273
ZUOG=ZU0(K)*ZU05*453.59/(30.48)**3.
MUPOS=MU(K)*14.882
30  WRITE (3,21) K,YDR,VELO,TK,ZUOG,ME(K),MUPOS
5   CONTINUE
ERROR=ABS((DISP(161)-DISP2)/DISP2)
IF (ERROR.LT.0.001) GO TO 9999
DISP(161)=DISP2
9   CONTINUE
14  FORMAT (/IX,I4,4E20.7)
20  FORMAT (/IX,I4,5E20.7)
21  FORMAT (IX,I3,6E18.5)
9999 STOP
END

```

C THIS SUBPROGRAM IS USED TO DETERMINE PRESSURE DISTRIBUTION
C ALONG THE NOZZLE AXIS

SUBROUTINE PRESS (PS,R,PO,A,DISP,P)

```

DIMENSION P(161),A(161),DISP(161)
P(1)=PS
DO 1 I=1,160
ARAT=(A(I+1)-DISP(I+1))/.05
CALL EXITP(R,PO,ARAT,PX)
P(I+1)=PX
RETURN
END

```

C THIS SUBPROGRAMME IS USED TO DETERMINE DISPLACEMENT THICKNESS

SUBROUTINE DISPLE (D,ZU0,DSIE,U,VES,TY,TTY,TY1,ME,DISP)

```

REAL ME(171)
DIMENSION U(161),DELY(161),DELY1(161),TY(161),
1 TY1(161),ZU0(161),VES(161)
TY(1)=0.
DISP=0.
TY1(160)=.2936
DO 8 J1=160,2,-1
DELY1(J1)=DSIE/((ZU0(J1)+ZU0(J1+1))/2*(U(J1)+U(J1+1))/2.)*12.*D
8 TY1(J1-1)=TY1(J1)-DELY1(J1)
DO 7 J=1,160
ME(J)=U(J)/VES(J)
DELY(J)=DSIE/((ZU0(J)+ZU0(J+1))/2*(U(K)+U(J+1))/2.)*12.*D
IF (U(J).EQ.U(J+1)) GO TO 9
U1=U(J)/U(161)*ZU0(J)/ZU0(160)
U2=U(J+1)/U(161)*ZU0(J)/ZU0(160)
DISP=DISP+((1-U1)+(1-U2))/2.*DELY(J)
TTY=TY(J)
9 TY(J+1)=TY(J)+DELY(J)
7 CONTINUE
RETURN
END

```

C THIS SUBPROGRAM IS USED TO PREDICT PRESSURE AT DISTANCE X
C FROM NOZZLE ENTRANCE (BY EFFECTIVE AREA) IF ISENTROPIC
C FLOW HAS BEEN ASSUMED ALONG THE NOZZLE

SUBROUTINE EXITP (R, P0, RD, PEXIT)

```
PE=0.001
H=1.
TOLER=0.00001
DE=((R-1)/2)**0.5*(2/(R+1))**((R+1)/(2*(R-1)))/RD
RE=(1-(PE/P0)**((R-1)/R))**0.5*(PE/P0)**(1/R)
IF (ABS((RE-DE)/DE).LE.TOLER) GO TO 53
IF (RE.GT.DE) GO TO 1
1 PEL=PE+H
2 REL=(1-(PEL/P0)**((R-1)/R))**0.5*(PEL/P0)**(1/R)
IF (ABS((REL-DE)/DE).LE.TOLER) GO TO 53
IF ((REL-DE).GT.0) GO TO 3
PE=PEL
GO TO 7
3 H=H/2
PEL=PE+H
GO TO 2
4 PEL=PE+H
10 REL=(1-(PEL/P0)**((R-1)/R))**0.5*(PEL/P0)**(1/R)
IF (ABS((REL-DE)/DE).LE.TOLER) GO TO 53
IF ((REL-DE).GT.0) GO TO 5
H=H/2
PEL=PE+H
GO TO 10
5 PE=PEL
GO TO 1
53 CONTINUE
PEXIT=PE
RETURN
END
```